Separation and Purification Technology 375 (2025) 133827

Contents lists available at ScienceDirect

Separation and Purification Technology

journal homepage: www.elsevier.com/locate/seppur

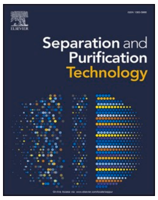

Structural modulation via mesoporous silica templating in covalent organic frameworks: Converting functional aspects for adsorption behavior

Yang-Chin Kao [a], Kuan-Ting Yeh [a], Mohamed Gamal Mohamed [a], Hira Karim [b], Wei-Hung Su [a], Shiao-Wei Kuo [a,c,*]

[a] *Department of Materials and Optoelectronic Science, Center of Crystal Research, National Sun Yat-Sen University, Kaohsiung 804, Taiwan*
[b] *Department of Chemistry, School of Natural Sciences (SNS), National University of Sciences and Technology (NUST), H-12, Islamabad 44000, Pakistan*
[c] *Department of Medicinal and Applied Chemistry, Kaohsiung Medical University, Kaohsiung 807, Taiwan*

ARTICLE INFO

Editor: Harvey Yi Huang

Keywords:
Mesoporous Silica
Covalent Organic Frameworks
Schiff-base Reaction
CO_2 Uptake
Dye Removal

ABSTRACT

This study investigates the influence of mesoporous silica templating on the structure and functionality of covalent organic frameworks (COFs) synthesized using 2,4,6-triformylphloroglucinol (TFP), triphenylamine (TPh), and tris(biphenyl)amine (TBPh) through Schiff-base reaction. COFs synthesized without (type I) and with (type II) mesoporous silica templates were characterized using FTIR, XPS, and solid-state NMR, revealing the successful formation of imine bonds and triazine units. Morphological analyses, including TEM, SEM, and XRD, exhibited that mesoporous silica templating significantly enhanced pore ordering and surface roughness. Nitrogen (N_2) adsorption/desorption measurements confirmed high surface areas (up to 904 m^2/g) with microporous structures. The mesoporous silica-templated materials to form type II CTF-based COFs exhibited superior CO_2 adsorption (3.46 mmol/g at 273 K) and rapid Rhodamine B (RhB) dye removal (> 99 % within 120 s), ascribed to their ordered structure and strong π-π interactions. These results demonstrate the role of mesoporous silica templating in tailoring structural properties to optimize the adsorption performance of COF materials, offering insights into designing advanced adsorbents for environmental remediation.

1. Introduction

The textile industry has grown rapidly in recent decades, becoming a cornerstone of modern economies. However, this growth has been accompanied by an extensive reliance on organic dyes, significantly contributing to wastewater pollution [1]. These dyes are visually unappealing and pose severe threats to aquatic ecosystems and human health due to their toxicity, persistence, and potential carcinogenicity [2–4]. On top of that, the large-scale production processes in the textile industry are energy-intensive, giving rise to substantial greenhouse gas emissions, particularly CO_2, which exacerbates global warming [5–7]. To mitigate these environmental challenges, developing materials capable of efficiently adsorbing both CO_2 [8–10]and organic dyes [11–19] has emerged as a critical research focus. Traditional adsorbents, such as amorphous porous materials, including activated carbon [20,21] and natural zeolites [22,23], have been widely used for such applications. While activated carbon offers high adsorption capacity and zeolites exhibit diverse crystalline structures, their versatility is limited in addressing a broad range of adsorption needs, thereby restricting their practical applications.

In response to these limitations, researchers have turned their attention to advanced porous materials, such as metal–organic frameworks (MOFs) [24–26], Conjugated microporous polymers [27–34], covalent organic frameworks (COFs) [27–46], and mesoporous silica [47–51]. Among these, COFs have garnered significant attention as an emerging class of organic polymers distinguished by their high specific surface areas, well-defined ordered porosity, robust frameworks, and excellent crystallinity [27–46]. A key advantage of COFs lies in their synthesis via reversible condensation reactions, which enable precise control over the selection of building blocks and the resulting framework structures [52–55]. This tunability allows for the design of COFs with tailored properties to meet specific functional demands, making them highly versatile for applications in environmental remediation, including gas storage [56], catalysis [57], and adsorption-based degradation of pollutants [58–60]. Looking forward, the development of COFs and other advanced porous materials offers an exciting pathway toward

---

* Corresponding author at: Department of Materials and Optoelectronic Science, Center of Crystal Research, National Sun Yat-Sen University, Kaohsiung 804, Taiwan.

E-mail address: kuosw@faculty.nsysu.edu.tw (S.-W. Kuo).

https://doi.org/10.1016/j.seppur.2025.133827
Received 1 April 2025; Received in revised form 19 May 2025; Accepted 29 May 2025
Available online 30 May 2025

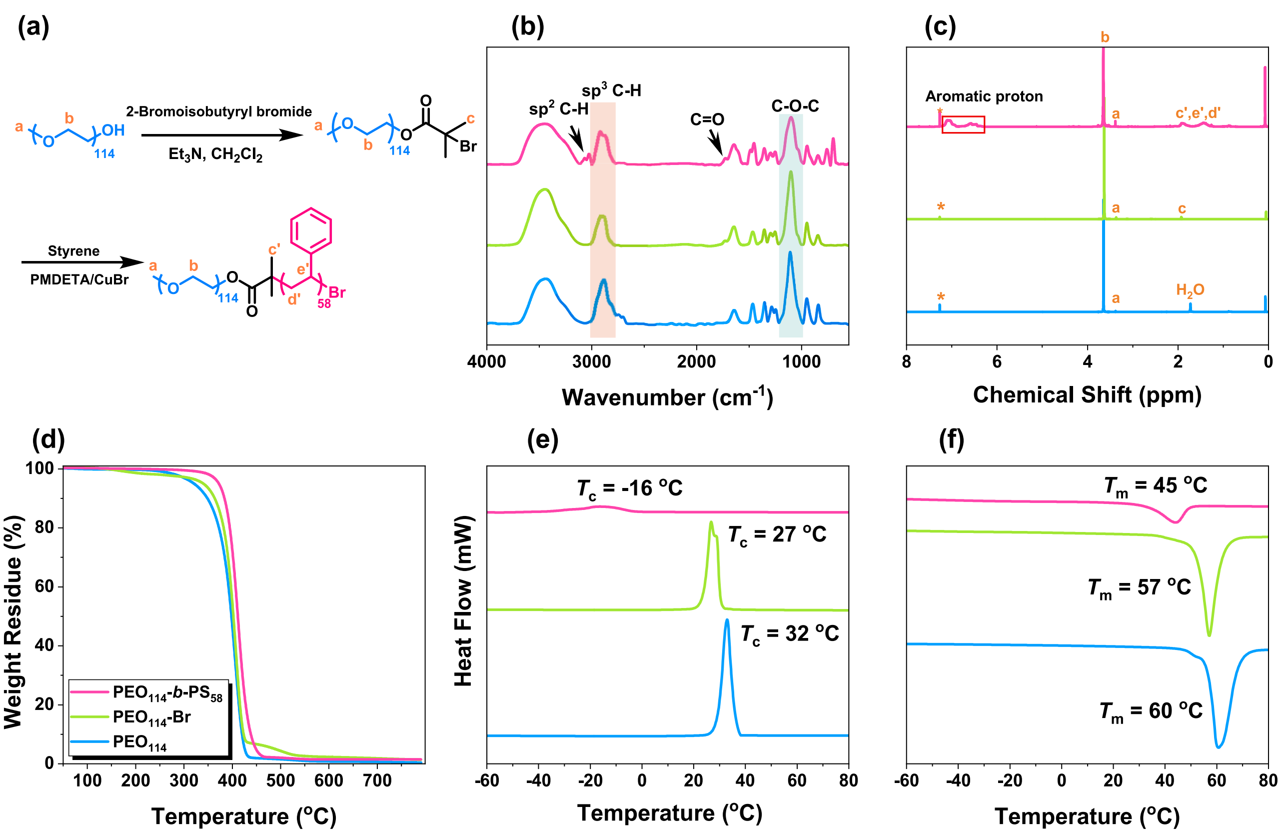

Fig. 1. (a) Synthesis route of PEO_{114}-*b*-PS_{58} and the corresponding (b) FTIR spectrum, (c) NMR spectrum (* is the peak for $CHCl_3$-*d*), (d) TGA analysis, and (e, f) DSC analysis of PEO_{114}, PEO_{114}-Br, and PEO_{114}-*b*-PS_{58}.

addressing the pressing environmental issues posed by the textile industry. Through continued research, these materials hold the potential to significantly reduce wastewater pollution and greenhouse gas emissions, paving the way for more sustainable industrial practices.

Recent advances in COF synthesis have leveraged dynamic and reversible reactions, such as triazine polymerization, Schiff-base condensation, and aldol condensation. Among these, covalent triazine frameworks (CTFs) have gained significant attention [61–64], and CTFs are distinguished by their nitrogen-rich functional groups, such as imine and triazine units, which serve as active sites for adsorption. These functional groups interact strongly with CO_2 due to the molecule's large quadrupole moment, facilitating dipole-quadrupole interactions and enhancing CO_2 capture efficiency [65]. Additionally, the large specific surface area of CTFs provides a high density of active sites, while N-π and π-π interactions between the framework and dye molecules enhance dye adsorption. The intrinsic π-π stacking of the conjugated structure also contributes to high porosity, allowing rapid dye adsorption and improved adsorption kinetics [66–68].

Unlike conventional two-dimensional (2D) COFs synthesized via bulk solvothermal methods, which frequently suffer from poor structural order and poorly defined porosity, our templating strategy enables precise control over key structural parameters, including pore dimensions, particle morphology, and interlayer stacking. The incorporation of a rigid silica template during the Schiff base condensation process plays a critical role in directing the growth of the COF, promoting uniform layer alignment, reducing structural defects, and enhancing π–π stacking interactions between layers. Following synthesis, the selective removal of the silica template preserves the integrity of the ordered pore network, resulting in COF materials that exhibit significantly improved crystallinity, mechanical robustness, and mass transport characteristics. Furthermore, by tuning the pore size and geometry of the silica template, we can systematically adjust the surface area, pore volume, and external morphology of the COFs. This level of structural tunability allows for the optimization of functional properties such as gas adsorption and dye uptake, all without necessitating changes to the chemical structure of the monomeric building blocks.

In this study, we propose the design and synthesis of these COFs using triazine-based structures: 4,4′,4′'-(1,3,5-triazine-2,4,6-triyl)trianiline (TPh-$3NH_2$) [69] and 4′,4′'',4′''''-(1,3,5-triazine-2,4,6-triyl)tris(([1,1′-biphenyl]-4 amine)) (TBPh-$3NH_2$) [70], in combination with the trialdehyde monomer 2,4,6-triformylphloroglucinol (TFP). The synthesis was carried out via acid-catalyzed Schiff-base polycondensation, incorporating a diblock copolymer to fabricate an ordered silica template [71,72]. The polymerization process, involving TFP and the two triazine-based monomers, was conducted in the presence of the mesoporous silica template to facilitate the formation of an ordered framework. Post-synthesis, the silica template was removed to yield a porous, crystalline COF structure. The structural changes resulting from this process were characterized using X-Ray Diffraction (XRD) analysis, which confirmed the successful formation of highly ordered frameworks. The incorporation of the mesoporous silica template during synthesis was found to enhance the structural regularity and porosity of the COFs, thereby improving their functional properties for applications in CO_2 capture and dye adsorption. By tailoring the building blocks and leveraging a mesoporous silica-templated synthesis approach, this study highlights a scalable strategy for creating highly ordered and functionalized COFs. These materials not only exhibit superior adsorption properties but also provide insights into the relationship between framework design and performance, paving the way for advancements in environmental remediation technologies.

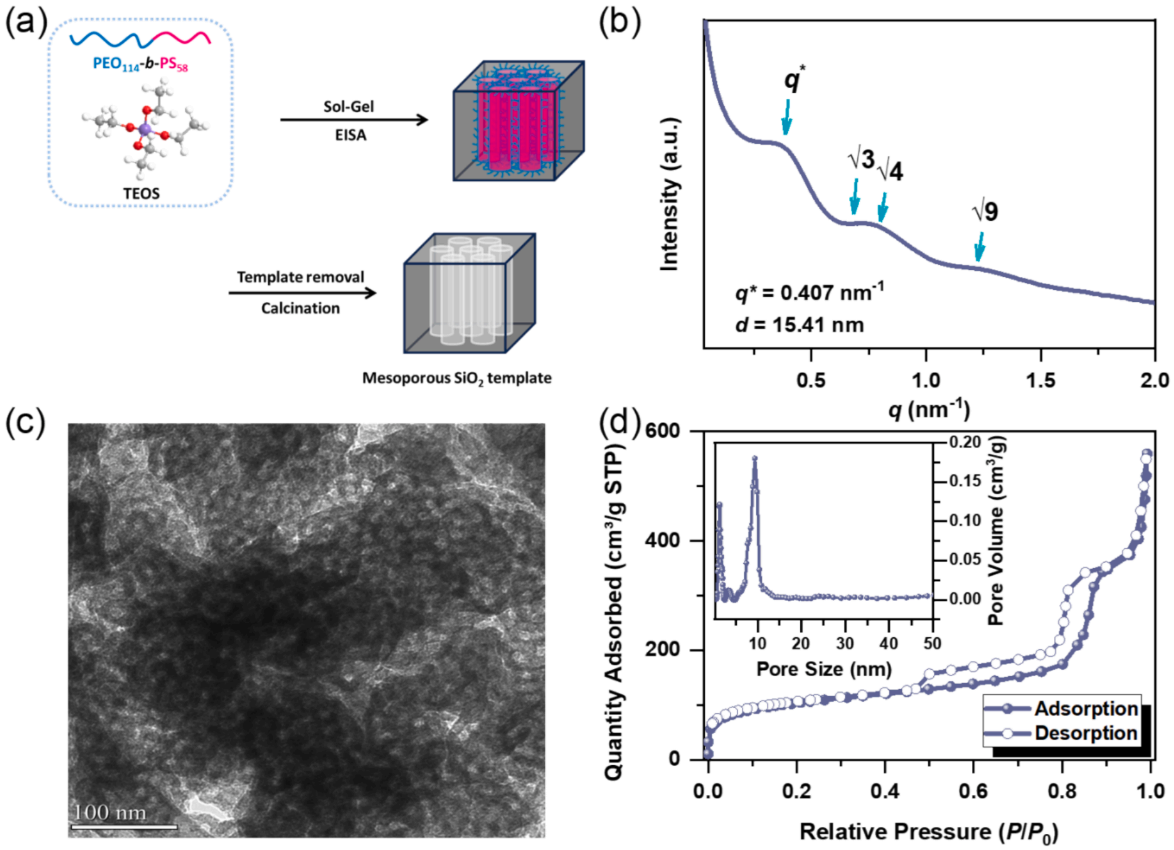

Fig. 2. (a) Preparation of mesoporous silica materials and the corresponding (b) SAXS pattern, (c) TEM image, (d) BET and pore size profiles of mesoporous silica materials.

2. Experimental Section

2.1. Materials

2-Bromoisobutyryl bromide (2-Br-IsoBuBr, 97 %), triethylamine (Et_3N, 99 %), styrene (Sty, 99 %), and copper(I) bromide (CuBr, 98 %) were purchased from Alfa Aesar. Tetraethyl orthosilicate (TEOS, 98 %), 1,2-dichlorobenzene (99 %), and 1-butanol (> 99 %) were purchased from ACROS. Acetic acid was purchased from Honeywell. Matrix Scientific was the supplier for 4-aminobenzonitrile (98 %). Hydrofluoric (HF) acid, 4-(4-aminophenyl)benzonitrile (95 %), dichloromethane, Rhodamine B (RhB, 95 %), N,N,N',N'',N''-Pentamethyldiethylene-triamine (PMDETA, 99 %), poly(ethylene glycol) methyl ether [PEO_{114}, $M_n = 5000$ g/mol] and 2,4,6-triformylphloroglucinol (TFP) were purchased from Sigma-Aldrich. 4,4′,4''-(1,3,5-triazine-2,4,6-triyl)trianiline ($TPh\text{-}3NH_2$) and 4′,4'''',4′''''-(1,3,5-triazine-2,4,6-triyl)tris(([1,1′-biphenyl]-4-amine)) ($TBPh\text{-}3NH_2$) were synthesized as displayed in Schemes S1 and S2.

2.2. Preparation of PEO-b-PS diblock copolymer

The macroinitiator PEO_{114}-Br was synthesized by dissolving 20 g of monomethoxy PEO_{114} in 90 mL of dry THF, followed by the addition of 1 mL of Et_3N to form a clear solution. After cooling the mixture in an ice-water bath, 0.92 g (4.0 mmol) of 2-Br-IsoBuBr was added dropwise over 30 min under constant stirring. The reaction was then maintained at 30 °C and stirred overnight. To isolate the product, the reaction mixture was poured into 300 mL of cold diethyl ether, and the resulting precipitate was collected by filtration, washed with more cold ether, and dried under reduced pressure, yielding PEO_{114}-Br as a white solid. For the block copolymerization, a typical procedure involved charging a flame-dried ampoule with PEO-Br (5 g, 0.97 mmol), CuBr (0.14 g, 0.97 mmol), PMDETA (0.17 g, 0.97 mmol), and Sty (5.86 g, 56.3 mmol). The mixture was degassed using three freeze–pump–thaw cycles, sealed under vacuum, and heated at 110 °C in an oil bath for 3 h. After cooling, the resulting viscous polymer solution was dissolved in 100 mL of THF and passed through a column of neutral alumina to remove residual copper. The final product, PEO_{114}-*b*-PS_{58}, was recovered by precipitation in 500 mL of petroleum ether, filtered, and dried under vacuum [Fig. 1**(a)**, Yield: 73 %].

2.3. Synthesis of mesoporous silica through an evaporation-induced self-assembly (EISA) process

To prepare the final material, transparent films were first formed by casting a homogeneous solution, prepared by stirring 1.5 g of TEOS and 0.35 g of HCl (0.1 M) into 7.5 g of PEO_{114}-*b*-PS_{58} solution in THF for 30 min, into Petri dishes and allowing the THF to evaporate at 25 °C for 48 h. The dried films were then ground into a fine powder and placed in an autoclave containing 45 mL of 1.0 M HCl, followed by hydrothermal treatment at 100 °C for 3 days. After washing and air drying, the material was calcined at 600 °C for 12 h with a heating rate of 1 °C/min, resulting in a white solid product [Fig. 2**(a)**].

2.4. Preparation of type I TFP-TPh and TFP-TBPh COFs

A total of 0.1 g of 2,4,6-triformylphloroglucinol (TFP) and either 0.16 g of $TPh\text{-}3NH_2$ or 0.27 g of $TBPh\text{-}3NH_2$ were combined in a 20 mL quartz ampoule along with 1,2-dichlorobenzene, 1-butanol, and 6 M acetic acid. The mixture was heated to 100 °C and maintained at this temperature for 72 h in an oil bath. During the heating process, TFP-TPh (I) and TFP-TBPh (I) were synthesized via Schiff-base reaction. The

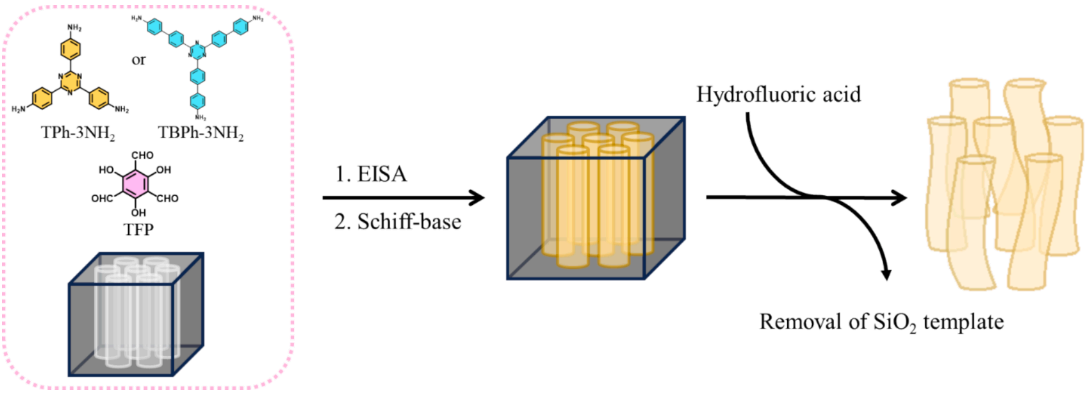

Scheme 1. Synthesis of (a) TFP-TPh COFs and (b) TFP-TBPh COFs with silica templates.

resulting solids were filtered and dried under a vacuum at 50 °C, yielding TFP-TPh (I) as a yellow powder with an 89 % yield and TFP-TBPh (I) with a 94 % yield.

2.5. *Preparation of type II TFP-TPh and TFP-TBPh COFs*

The mesoporous silica template (0.13 g or 0.18 g) was mixed with 0.1 g of TFP and either 0.16 g of TPh-3NH_2 or 0.27 g of TBPh-3NH_2. The mixture was packed into a 20 mL quartz ampoule along with the solvents 1,2-dichlorobenzene, 1-butanol, and 6 M acetic acid. The sealed ampoule was heated to 100 °C and maintained at this temperature for 72 h in an oil bath. After polymerization, the TFP-based hybrids were collected via reduced-pressure filtration. The residues were then treated overnight with 5 wt% HF for 24 h to remove the mesoporous silica template. The resulting material was washed multiple times with deionized water and ethanol, followed by vacuum drying in an oven at 70 °C. TFP-TPh (II) and TFP-TBPh (II) COFs were obtained with a yield of 64 % [Scheme 1].

3. Results and Discussion

3.1. *Synthesis and structural Characterization of TPh-3NH_2, TBPh-3NH_2 monomers*

We have synthesized TPh-3NH_2 and TBPh-3NH_2 monomers, and their chemical structures were confirmed through FTIR, ^{1}H NMR, and TGA analyses, as evident in **Figs. S1-S6**. Briefly, the absorption bands for both synthesized compounds, which share similar structural features, are centered around 1620 and 1365 cm^{-1}, corresponding to the presence of triazine units. Additionally, TPh-3NH_2 exhibited NH_2 stretching bands at 3462 and 3322 cm^{-1}, while TBPh-3NH_2 showed bands at 3429 and 3347 cm^{-1} (**Figs. S1 and S4**). The ^{1}H NMR spectrum of TPh-3NH_2 [**Fig. S2**] displayed the proton signals at 8.34, 6.68, and 5.90 ppm, corresponding to aromatic protons and NH units, respectively. Similarly, TBPh-3NH_2 [**Fig. S5**] showed the proton signals at 8.70, 7.82, 7.54, 6.70, and 5.47 ppm, which are also attributed to aromatic protons and NH units. Thermal analysis revealed that the T_{d10} values (temperature at which 10 % weight loss occurs) for TPh-3NH_2 and TBPh-3NH_2 were

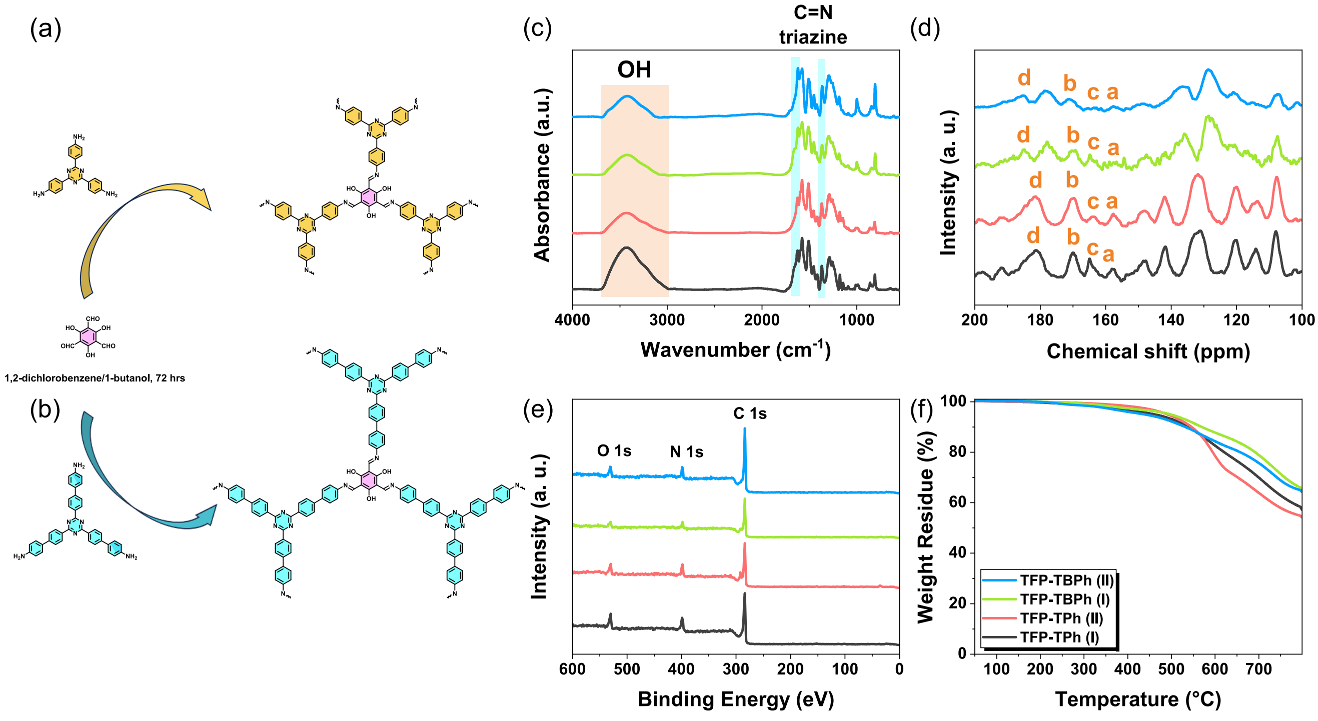

Fig. 3. Synthesis of (a) TFP-TPh COFs and (b) TFP-TBPh COFs by the Schiff-base reaction and the corresponding (c) FTIR spectrum, (d) solid-state ^{13}C NMR analysis, (e) XPS spectra and (f) TGA profiles.

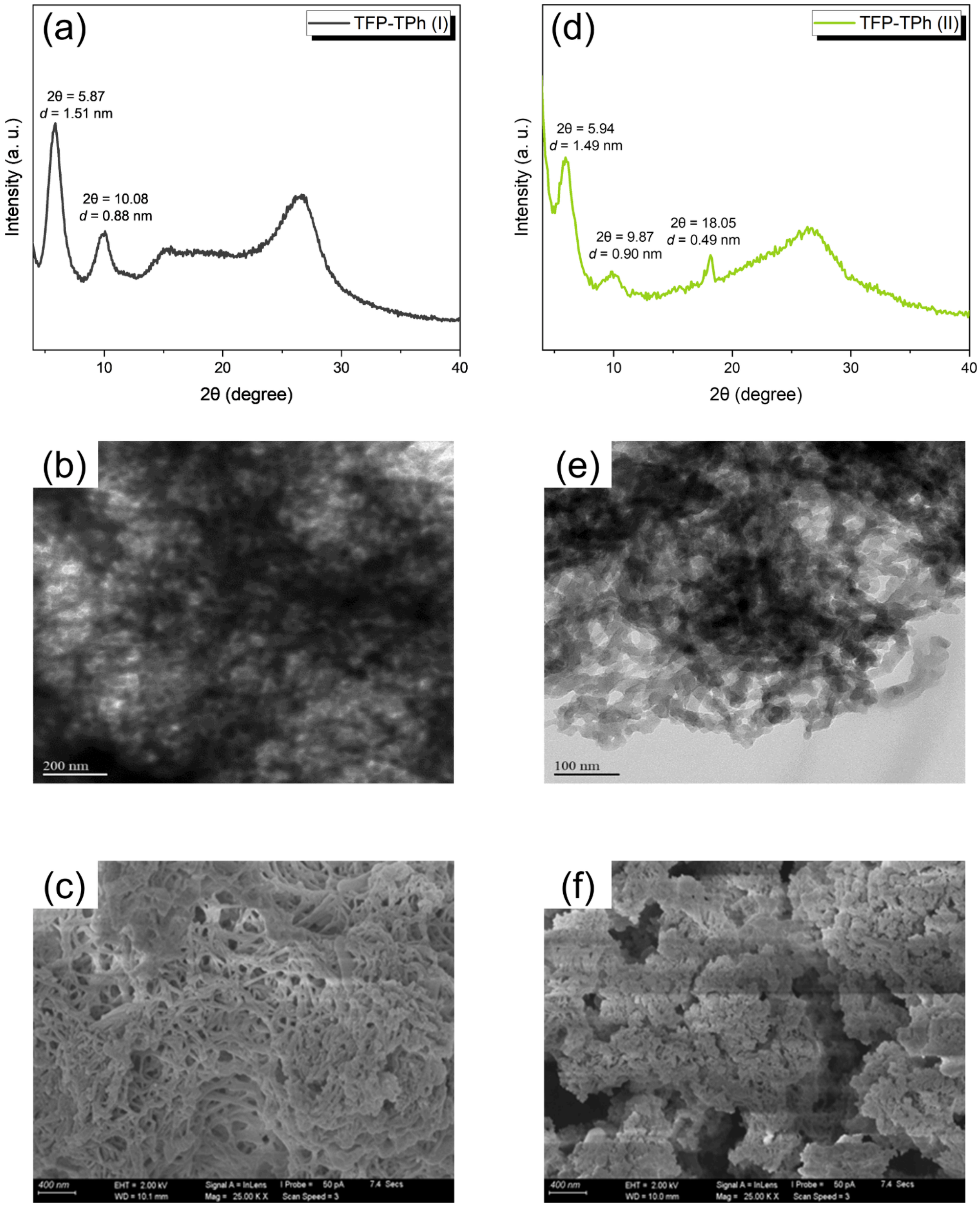

Fig. 4. XRD spectra, TEM images, and SEM images of TFP-TPh (I): (a), (b), (c); TFP-TPh (II): (d), (e), (f).

468 °C and 492 °C, respectively. The corresponding char yields were 50.6 wt% and 33.4 wt%, as indicated in **Figs. S3 and S6**.

3.2. *Mesoporous silica material by using PEO-b-PS diblock copolymer as template*

We synthesized PEO_{114}-*b*-PS_{58} diblock copolymer through ATRP (Fig. 1**(a)**), which was corroborated by FTIR, ^{1}H NMR, TGA, and DSC analyses, as shown in Fig. 1. The FTIR spectrum of PEO_{114}-*b*-PS_{58} unveiled 3071, 3028, 2920, 1728, and 1103 cm^{-1}, corresponding to the presence of sp^2 C—H, sp^3 C—H, C=O, and C—O—C units, respectively [Fig. 1**(b)**]. Furthermore, the ^{1}H NMR spectrum [Fig. 1(c)] displayed the proton signals at 6.46–7.09 and 1.91–1.85 ppm, corresponding to aromatic protons and aliphatic protons of PS segment, 3.64 and 3.38 ppm are due to the main chain of $OC\underline{H}_2$ and the chain end of $OC\underline{H}_3$ of PEO segment.

From the integrated area of aromatic protons of the PS segment and $OC\underline{H}_2$ of the PEO segment, we can calculate the molecular weight of the PS segment. **Table S1** lists the molecular weights and polydispersity index (PDI). Thermal analysis of the PEO_{114}-*b*-PS_{58} diblock copolymer indicated that the T_{d10} value was 383 °C based on TGA analyses in Fig. 1 **(d)**, the crystallization temperatures (T_c) and the melting point (T_m) of were determined to be −16 °C and 45 °C of PEO segment as shown in Fig. 1**(e) and (f)**, which all strongly affected by the microphase separation and nano-confined effect of PEO segment after covalent bonded PS segment when compared with pure PEO and PEO-Br segment.

We prepared the mesoporous silica materials by using PEO_{114}-*b*-PS_{58} diblock copolymer as the template by utilizing the microphase separation and EISA processes and then fabricated the well-defined mesoporous silica at 600 °C to remove PEO_{114}-*b*-PS_{58} diblock copolymer as displayed in Fig. 2**(a)**. The self-assembled mesoporous silica was thoroughly characterized using a combination of analytical techniques, including IR, TGA, XRD, SAXS, TEM, and BET surface area analysis. The IR spectrum revealed a characteristic absorption band at 1080 cm^{-1}, which is attributed to the stretching vibration of the Si-O-Si framework, as shown in **Fig. S7**. Thermogravimetric analysis (**Fig. S8**) indicated high thermal stability, with a 10 % weight loss temperature (T_{d10}) observed at 753 °C and a residual weight of 89.2 wt%, confirming the

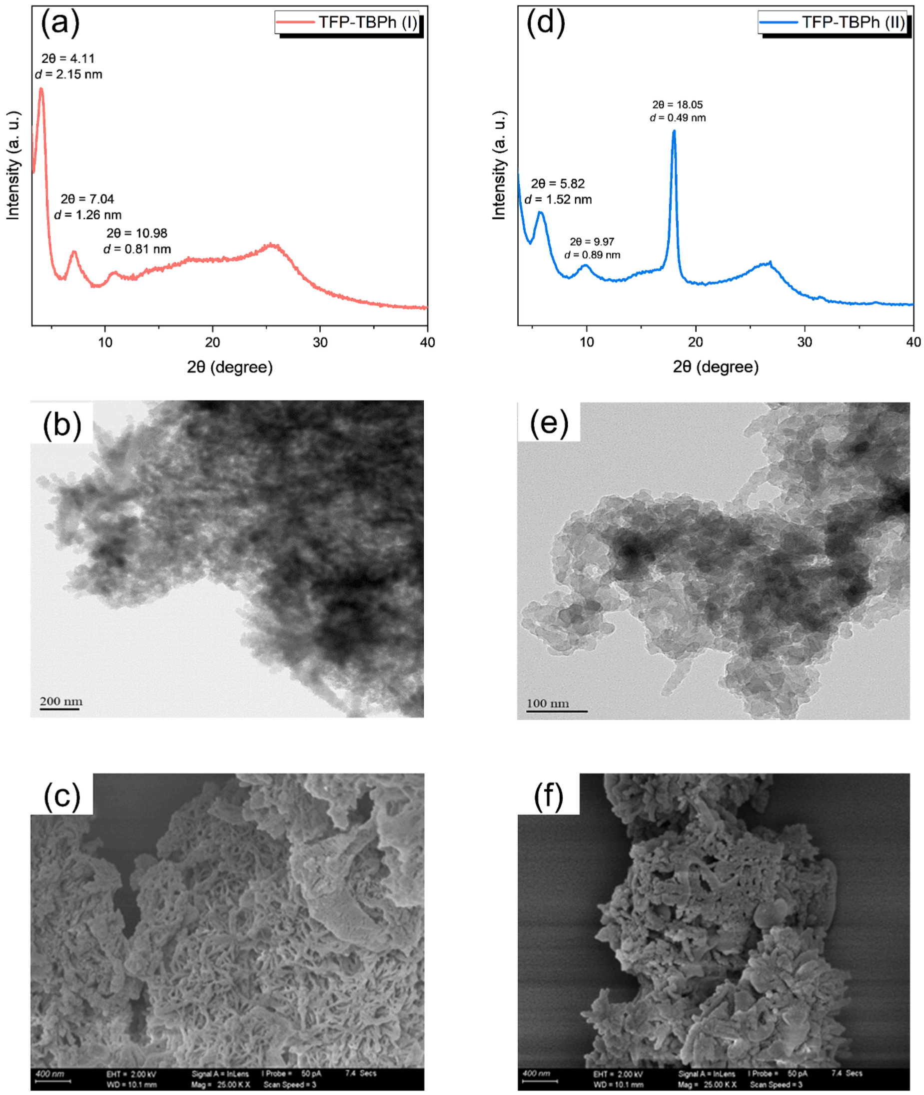

Fig. 5. XRD spectra, TEM images, and SEM images of TFP-TBPh (I): (a), (b), (c); TFP-TBPh (II): (d), (e), (f).

robust nature of the mesoporous silica structure. Fig. 2**(b)** shows the SAXS pattern of mesoporous silica with peak ratios of $1{:}\sqrt{3}{:}\sqrt{4}{:}\sqrt{9}$, indicating the existence of the hexagonally packed cylinder (HPC) structure, which could be confirmed by the TEM image as shown in Fig. 2**(c)**. The *d*-spacing of mesoporous HPC silica was 15.41 nm from the first q^* peak ($q = 0.407\ \mathrm{nm}^{-1}$) based on the Bragg law ($d = 2\pi/q^*$). However, XRD analysis showed amorphous peaks in **Fig. S9**. Fig. 2**(d)** shows N_2 adsorption/desorption isotherms recorded at 77 K, indicating the typical type IV curve with H_1 hysteresis loop with a value of P/P_0 from 0.4 to 0.8 for the capillary condensation step, indicating a cylindrical-like mesoporous structure. The specific surface area (S_{BET}) of 383.4 $m^2\ g^{-1}$ was calculated, and the mean pore size was observed at 9.4 nm, determined from the Harkins and Jura model, which is consistent with SAXS and TEM results.

3.3. Synthesis and structural characterization of TFP-TPh and TFP-TBPh COFs

As illustrated in Fig. 3**(a)–(b)**, TFP underwent the Schiff-base reaction with TPh-3NH$_2$ and TBPh-3NH$_2$, resulting in two COF materials designated as TFP-TPh (I) and TFP-TBPh (I) COFs. In comparison, TFP-TPh (II) and TFP-TBPh (II) COFs were synthesized using mesoporous silica as a template and then treated overnight with 5 wt% hydrofluoric (HF) acid to remove the mesoporous silica template. The chemical structures of these four COF materials, collectively referred to as TFP-based COFs, were confirmed by FTIR, XPS, and solid-state ^{13}C NMR spectroscopy. The FTIR spectra of TFP-TPh and TFP-TBPh COFs are shown in Fig. 3**(c)**, revealing consistent characteristic peaks: a stretching vibration around 3435 cm^{-1} attributed to the phenolic unit from the TFP unit, a peak near 1620 cm^{-1} corresponding to the imine bond formed after the Schiff-base reaction, and the peaks around 1365 and 1575 cm^{-1} associated with the C═N stretching of the triazine ring units. Notably, both TFP-TPh and TFP-TBPh hybrids that have not undergone HF treatment to remove the silica template exhibit an additional peak at 1090 cm^{-1}, corresponding to the Si-O-Si units. However, after HF treatment, this peak vanishes, yielding the final TFP-TPh (II) and TFP-TBPh (II) COFs, as shown in **Fig. S10**. In the solid-state ^{13}C NMR spectra, signals within the range of 100–200 ppm were predominantly assigned to carbon atoms in the phenyl units. For TFP-TPh COFs, a peak at 157 ppm (aromatic C-OH) provided evidence of a successful Schiff-base reaction, while a peak at 169 ppm (C═O) indicated the presence of tautomeric structures, as shown in **Scheme S3(a)**. On top of that, a peak at 169 ppm corresponded to C═O bonds, and a peak at 181 ppm was assigned to C═N bonds, further corroborating the structural composition. Similarly, for TFP-TBPh COFs, a peak at 157 ppm (C═N) corroborated with the successful Schiff-base reaction, while a peak at 164 ppm (C═C) suggested tautomeric structures, as shown in **Scheme S3(b)**. Peaks observed at 169–171 ppm were attributed to C—O bonds,

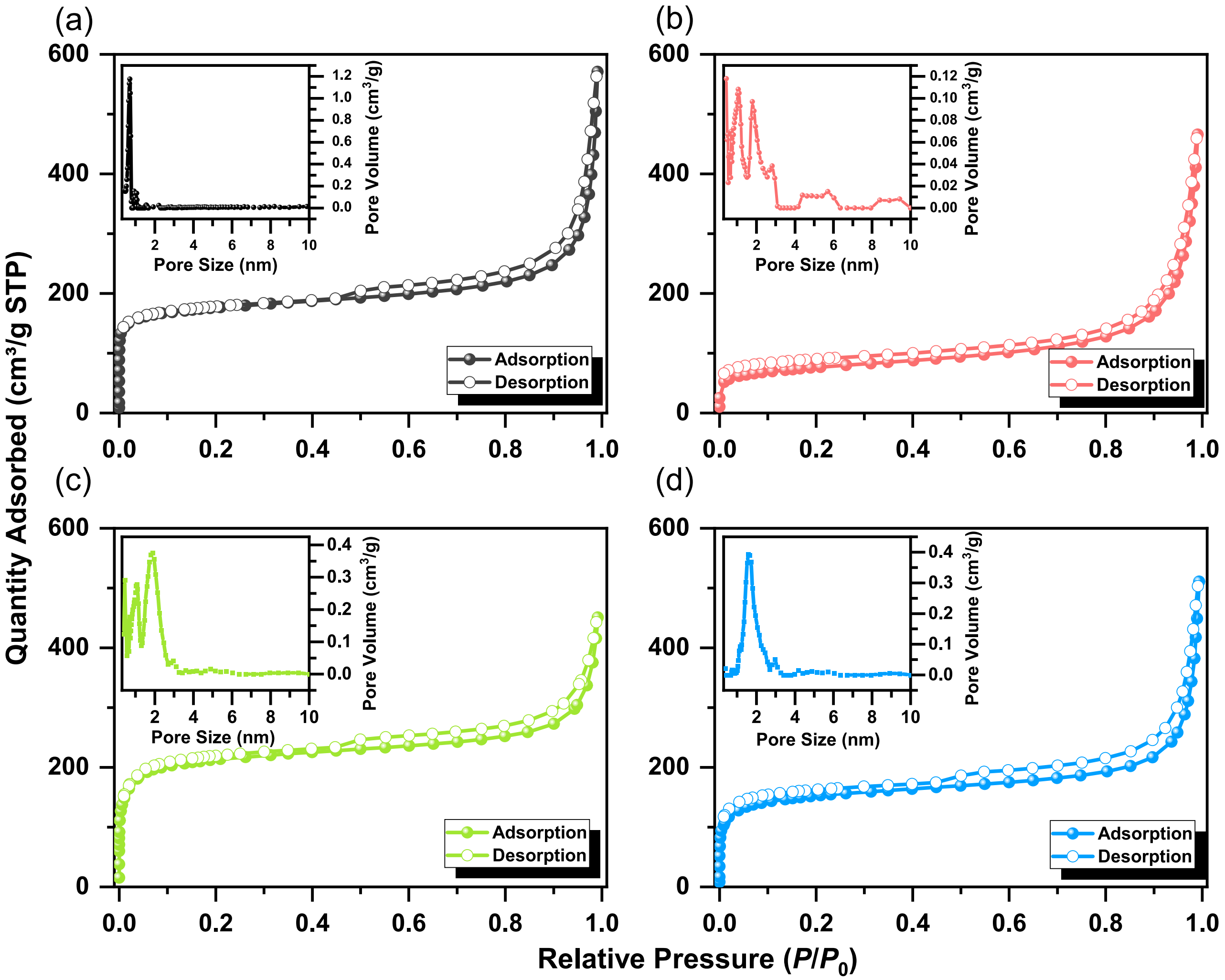

Fig. 6. N_2 adsorption/desorption isotherms and pore size distribution of (a) TFP-TPh (I), (b) TFP-TBPh (I), (c) TFP-TPh (II) and (d) TFP-TBPh (II).

and those at 184–185 ppm were assigned to C=O bonds. The differences in the spectra between TFP-TPh COFs and TFP-TBPh COFs can be attributed to the varying number of phenyl rings in TPh and TBPh, highlighting their distinct structural characteristics. The XPS analyses further elucidated the elemental composition and surface chemistry of the TFP-based COFs. As shown in Fig. 3**(e)**, the XPS spectra indicate signals for C 1s, N 1s, and O 1s, with the C 1s signal being significantly more intense than the N 1s and O 1s signals, consistent with elemental analysis. Notably, the absence of Si 2p signals in the 101–103 eV range confirms that the silica template has been successfully removed. The deconvoluted C 1s spectra of the TFP COFs revealed two primary peaks at 284.2 and 286.1 eV [**Fig. S11**], attributed to aromatic C=C and C=N bonds, respectively.

Notably, the C=C peak in TFP-TBPh COFs appeared more prominent than in TFP-TPh COFs due to the additional phenolic groups present in TFP-TBPh COFs. Similarly, the deconvoluted N 1s spectra displayed two peaks at 398.3 and 399.5 eV, corresponding to triazine ring and imine bonds, respectively [**Fig. S12**]. The triazine rings containing three C=N bonds are expected to contribute more significantly to the signal intensity compared to the imine bonds. Additionally, thermal analysis demonstrated the excellent thermal stability of these TFP-based COF materials. The T_{d10} values for TFP-TPh (I), TFP-TBPh (I), TFP-TPh (II), and TFP-TBPh (II) were 538, 569, 546, and 532 °C, respectively, with corresponding char yields of 57.2, 64.6, 54.2, and 64.3 wt% as shown in Fig. 3**(f)**. The morphological characteristics of these TFP-based COFs were analyzed using transmission electron microscopy (TEM), field-emission scanning electron microscopy (FE-SEM), and X-ray diffraction (XRD) analyses. TFP-TPh (I) and TFP-TBPh (I) COFs demonstrated fibrous structures, while TFP-TPh (II) and TFP-TBPh (II) COFs, synthesized with the addition of the mesoporous silica template, demonstrated more defined and organized morphologies compared to their template-free counterparts. This distinction is evident in the TEM images shown in Fig. 4**(b), (e)**, Fig. 5**(b), and (e)**. The original structure resembled popcorn or fibers; nevertheless, after incorporating a mesoporous silica template, it transformed into a cylinder worm-like morphology. SEM images further confirmed this transformation in the TFP COFs (II), as illustrated in Fig. 4**(c), (f)**, Fig. 5**(c), and (f)**. In the unprocessed TFP-TPh and TFP-TBPh hybrids, the XRD patterns exhibited amorphous characteristics in **Fig. S13**. Nevertheless, after HF treatment, TFP-TPh (II) and TFP-TBPh (II) displayed well-defined diffraction peaks. XRD analysis showed a new peak at 18.05° in TFP-TPh (II) COF owing to the inclusion of the mesoporous silica template. In the XRD patterns of TFP–TPh COFs [Fig. 4**(a, d)**], TFP–TPh (II) exhibits diffraction peaks at 5.94° and 9.87°, whereas the non-templated TFP–TPh (I) shows peaks at 5.87° and 10.08°, indicating a noticeable shift in layer stacking. Similarly, for the TFP–TBPh series [Fig. 5**(a, d)**], TFP–TBPh (II) presents peaks at 5.82° and 9.97°, while TFP–TBPh (I) displays reflections at 4.11°, 7.04°, and 10.98°, reflecting a significant reorganization of the π-π stacking upon templating. These results imply that the mesoporous silica template influenced the polymerization process by modifying the π-π stacking interactions and promoting the formation of a more ordered 3D structure between layers. This effect is particularly evident from the

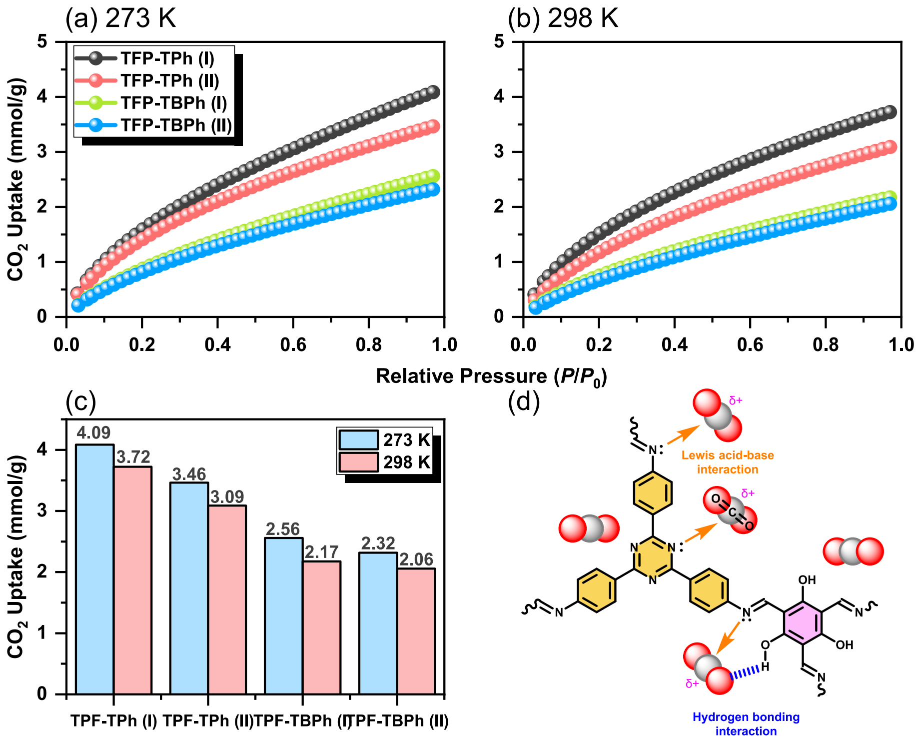

Fig. 7. CO_2 adsorption profiles of TFP COFs at (a) 273 K, (b) 298 K, and (c) summarize their corresponding CO $_2$ uptake values. (d) Proposed mechanism of CO_2 adsorption in TFP-Based COFs.

appearance of a peak at 18.05°.

The surface area and pore structures of these TFP-based COFs were evaluated using N_2 adsorption/desorption isotherms. As shown in Fig. 6 **(a)–(d)**, all these TFP-based COFs exhibited type IV isotherms with desorption hysteresis loops, indicative of materials with both microporous and mesoporous features. The N_2 adsorption curves showed a sharp increase at P/P_0 values of 0–0.03, followed by a more gradual rise between 0.03 and 0.05. The hysteresis loops observed in the 0.4–0.9P/P_0 range further confirmed the coexistence of micropores and mesopores. Using the Brunauer–Emmett–Teller (BET) model, the specific surface areas of TFP-TPh (I), TFP-TPh (II), TFP-TBPh (I), and TFP-TBPh (II) COFs were calculated as 839, 725, 904, and 711 $m^2\ g^{-1}$, separately. For TFP-based hybrids were calculated as 571 and 343 $m^2\ g^{-1}$ in **Fig. S14**. Pore size distribution and pore volume, determined via non-local density functional theory (NLDFT), are summarized in **Table S2**. The pore size distributions are confirmed microporous structures with predominant pore sizes of 1.2, 1.1, 1.9, and 1.6 nm for TFP-TPh (I), TFP-TPh (II), TFP-TBPh (I), and TFP-TBPh (II), respectively, highlighting their microporous nature. The TFP-based type II COFs exhibited relatively slightly lower surface area and smaller pore size compared with TFP-based type I COFs, probably because of more π-π stacking interactions and promoting the formation of a more ordered 3D structure between layers, which is consistent with XRD analyses.

The molecular electrostatic potential (MESP) maps of the TFP–TPh and TFP–TBPh COF building units reveal the reactive hotspots responsible for guest binding in **Fig. S15** [73,74]. In these maps, red regions correspond to areas of high electrostatic potential, typically localized around electronegative atoms such as the nitrogen of triazine, indicating potential nucleophilic sites. Conversely, blue regions denote areas of lower electron density, such as the amine hydrogen atoms, which serve as electrophilic sites. The juxtaposition of these high– and low–potential zones highlights the complementary binding sites within the COF framework, suggesting strong interactions with both CO_2 and cationic RhB dye molecules. Taken together, the MESP analysis confirms that these COFs possess appropriately distributed reactive centers, making them ideal candidates for efficient gas capture and dye adsorption.

3.4. Adsorption performance analyses of TFP-TPh and TFP-TBPh COFs

Ascribed to their high BET surface areas, all TFP-based COFs were anticipated to indicate excellent performance in CO_2 capture and dye adsorption. CO_2 adsorption measurements were carried out at 273 K and 298 K, as demonstrated in Fig. 7**(a) and 7(b)**. At 298 K, the CO_2 uptake capacities of TFP-TPh (I) and TFP-TPh (II) were 3.72 and 3.09 mmol g^{-1}, while TFP-TBPh (I) and TFP-TBPh (II) achieved 2.08 and 2.06 mmol g^{-1}, respectively. At 273 K, the CO_2 adsorption capacities increased across all samples, with TFP-TPh (I) and TFP-TPh (II) reaching 4.09 and 3.46 mmol g^{-1}, and TFP-TBPh (I) and TFP-TBPh (II) achieving 2.46 and 2.32 mmol g^{-1}, respectively, as summarized in Fig. 7**(c)**. The exceptional CO_2 adsorption performance can be attributed to the high specific surface areas, abundant micropores, and the presence of triazine units, which provide active sites for CO_2 capture. Notably, TPh-based TFP COFs demonstrated higher CO_2 uptake than TBPh-based TFP COFs, likely ascribed to the smaller molecular size of TPh. These findings indicate that the TFP-TPh COF has stronger interaction than TFP-TBPh COFs, and thus, this smaller size with fewer phenyl units facilitates stronger dipole-quadrupole interactions with the triazine units and strengthens hydrogen bonding with the phenolic units in TFP, as illustrated in Fig. 7 **(d)**. In addition, the TFP-based type II COFs exhibited slightly lower CO_2 adsorption capacity because of the relatively slightly lower surface area and smaller pore size compared with TFP-based type I COFs.

Quantum Theory of Atoms in Molecules (QTAIM) provides a powerful framework for characterizing intermolecular interactions, such as hydrogen bonding, electrostatic attraction, and Van Der Waals forces, by identifying bond critical points (BCPs) and evaluating their topological parameters [75,76]. At each BCP, key metrics including the electron density (ρ), its Laplacian ($\nabla^2\rho$), the potential energy density (V_r), the total energy density (H_r), and the ratio of the local kinetic energy density to the potential energy density ($-G/V_r$) are computed. These quantitative descriptors reveal both the strength and the nature of

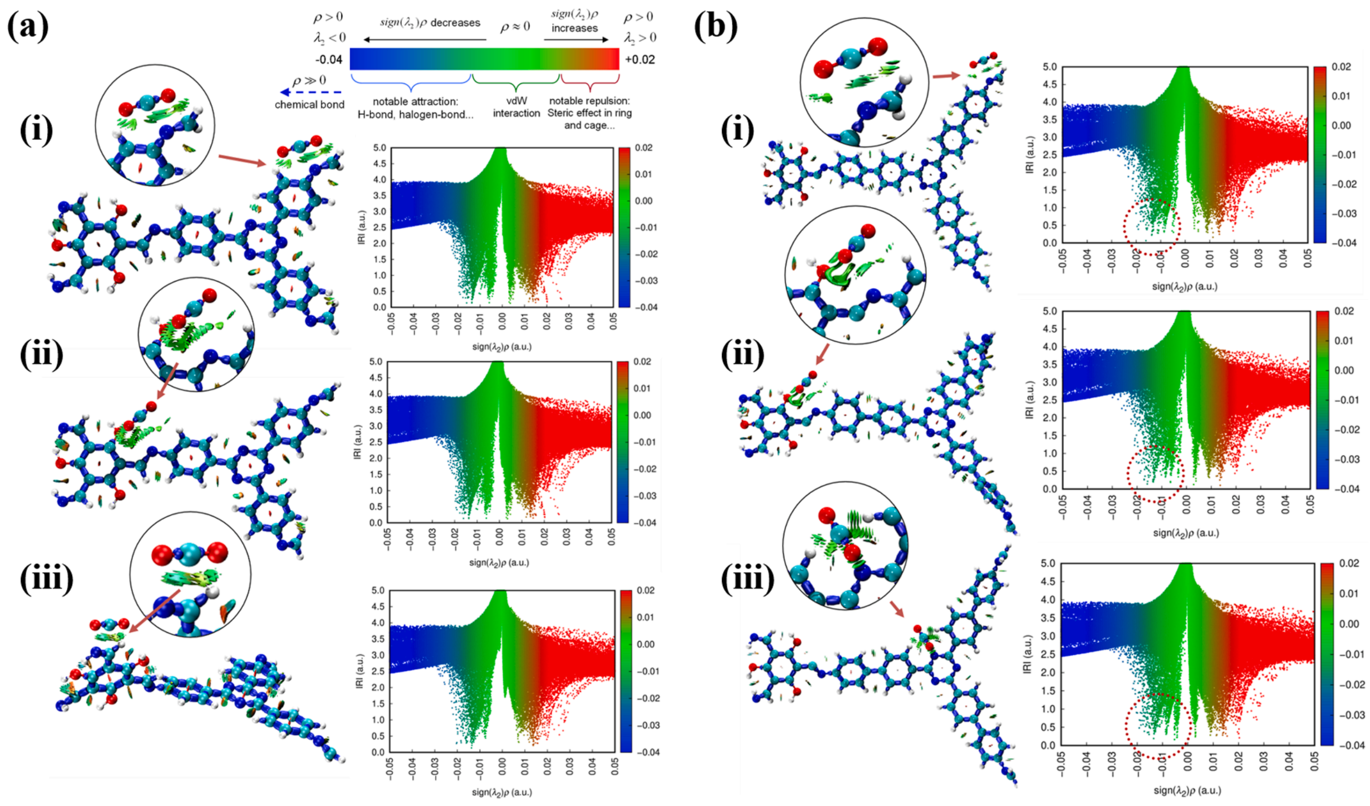

Fig. 8. The 3D isosurfaces and 2D scatter graphs of (a) TFP-TPh@CO$_2$ and (b) TFP-TBPh@CO$_2$ complexes.

the interaction.

The nature of these interactions was elucidated by examining the ρ and its $\nabla^2\rho$ at each bond critical point (BCP). A negative $\nabla^2\rho$ value indicates electron accumulation characteristic of shared–type (covalent) bonding, whereas a positive $\nabla^2\rho$ signifies electron depletion consistent with closed–shell (noncovalent) interactions [77–79]. In our QTAIM analysis [Fig. S16, Table S3], we identified three potential CO$_2$ binding sites [(i), (ii), and (iii)], corresponding to interactions with the amine units and hydrogen atoms in each unit of TFP COF. For all labeled N-C contacts between CO$_2$ and the COF framework, the electron density ρ at the BCPs was positive and maximal, indicating noncovalent interaction. The associated H_r was also positive, further confirming electrostatic rather than covalent bonding (covalent interactions yield negative H_r). Specifically, for the TFP-TPh@CO$_2$ interactions, both $\nabla^2\rho$ and H_r values were positive, and the ratio $-G_r/V_r$ exceeded 1, signaling dominant electrostatic and open-shell interactions over shared-shell (covalent)

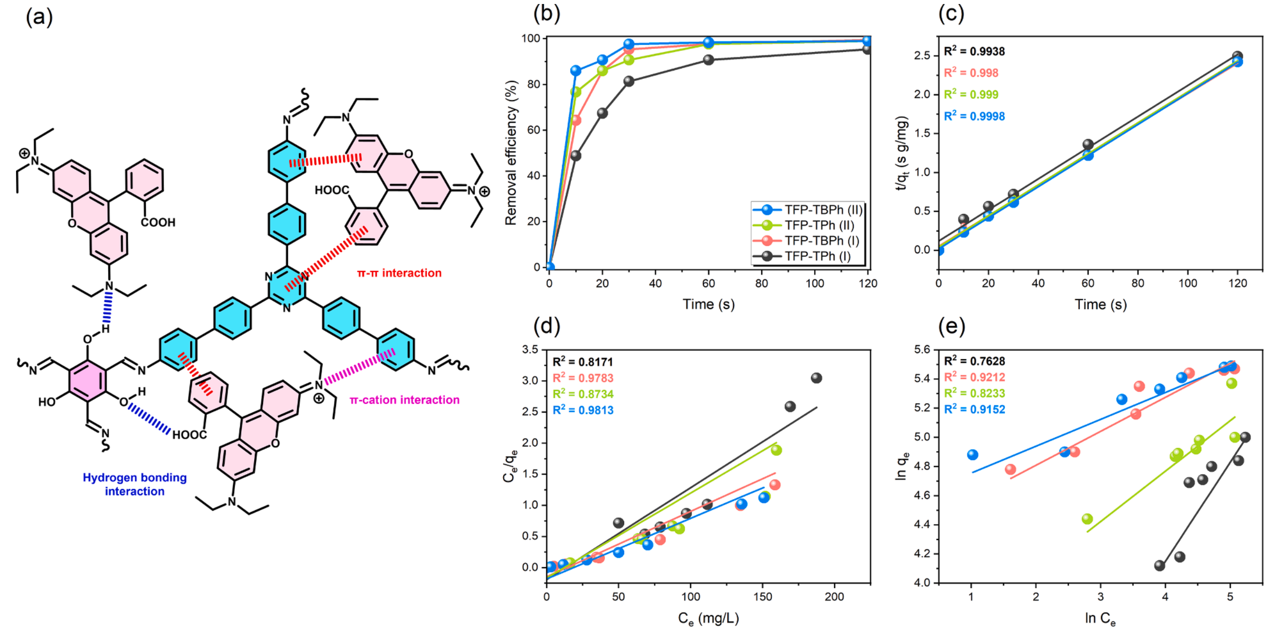

Fig. 9. (a) Possible RhB adsorption mechanisms of TFP COFs; (b) removal efficiency of aqueous RhB at different times after the addition, (c) pseudo-second-order kinetic fitting, (d) Langmuir fitting, and (e) Freundlich fitting of TFP COFs.

interactions. A similar trend was observed for TFP-TBPh@CO$_2$ contacts: positive $\nabla^2\rho$ and H_r values with $-G_r/V_r > 1$ indicate noncovalent attraction between the amine units and CO$_2$ [80]. These results collectively demonstrate that CO$_2$ binding in TFP COFs is governed primarily by strong electrostatic interactions rather than by covalent bond formation.

3.5. Interaction Region Indicator (IRI) analysis

To elucidate the nature of weak intermolecular contacts between COF subunits and guest molecules, we applied the Interaction Region Indicator (IRI) method. IRI is defined as

$$\boldsymbol{IRI}(\boldsymbol{r}) = \frac{\nabla\boldsymbol{\rho}(\boldsymbol{r})}{[\boldsymbol{\rho}(\boldsymbol{r})^{a}]}$$

and relies solely on the electron density (ρ) and its gradient. By coloring the resulting isosurfaces according to the sign of the second Hessian eigenvalue (λ_2) multiplied by ρ, one can distinguish attractive Van Der Waals interactions (green), hydrogen bonds (blue), and steric repulsion (red) in a single representation [81]. In the TFP COF@CO$_2$ systems, the IRI isosurfaces (Fig. 8) reveal extensive green regions between the CO$_2$ oxygen atoms and the hydrogen atoms of both TPh and TBPh units, confirming that dispersion forces dominate the CO$_2$ binding at all three investigated sites [(i)-(iii)]. The corresponding 2D scatter plots of sign $(\lambda_2)\rho$ versus IRI display characteristic peaks near zero, reinforcing the conclusion that Van Der Waals interactions are the primary stabilizing force. Notably, the TFP-TBPh@CO$_2$ complexes exhibit sharper and more condensed peaks (around -0.01 to -0.02 a.u.) compared to TFP-TPh@CO$_2$, indicating that the extended biphenyl surface of TBPh enhances dispersion binding strength.

In aquatic environments, the adsorption of organic pollutants is governed by several factors, including Lewis acid-base interactions [82], hydrogen bonding interactions [66–72,82], and π-π interactions [83–85] between the adsorbent and the dye. These interactions escalate the physical or chemical bonding between the adsorbent and the dye molecules. In addition to their CO$_2$ adsorption capabilities, TFP-based COFs are also highly effective in adsorbing organic dyes, addressing both air pollution and water contamination challenges. To evaluate the dye adsorption performance of TFP-based COFs, we conducted experiments using RhB solutions. The remaining RhB concentration in solution was monitored via ultraviolet–visible (UV–Vis) spectroscopy by measuring absorbance over a time range of 0–120 s. RhB aqueous solutions reveal a characteristic absorbance peak at 552 nm, which was used for quantitative analysis [**Fig. S17 and Tables S4-S7**]. Adsorbents (5 mg) were introduced into RhB solutions (10 mL, 25 mg L^{-1}), and all four adsorbents nearly decorated the dark pink RhB solution to colorless within 120 s. The decrease in absorbance verified that effective adsorption and equilibrium adsorption capacities (q$_e$) were calculated. At 10 s, TFP-TPh (I) and TFP-TBPh (I) COFs achieved removal efficiencies of 48.83 %, while TFP-TPh (II) COF reached 76.74 %, and TFP-TBPh (II) COF demonstrated the fastest performance, achieving 86.04 %. By 30 s, TFP-TBPh (II) COF removed 97.67 % of RhB. At 120 s, TFP-TPh (I) achieved a removal efficiency of 95.35 %, while the other three adsorbents removed over 99 % of RhB, as shown in Fig. 9 **(b)**. The adsorption kinetics were analyzed using the pseudo-second-order kinetic model proposed by Ho and McKay [86–88]. As shown in Fig. 9**(c)** and **Table S8**, the fitting degrees (R^2) for all four COF adsorbents were above 0.99. The rate constants (k_2) followed the trend: TFP-TBPh (II) > TFP-TPh (II) > TFP-TBPh (I) > TFP-TPh (I) COFs, with values of 1.116, 0.492, 0.436, and 0.180 g mg^{-1} min^{-1}, distinctively.

The superior performance of type II TFP-based COF adsorbents compared to type I can be attributed to the incorporation of the mesoporous silica template, which altered the structural framework, enhancing dye penetration into the pore channels and promoting more efficient chemisorption. Additionally, the enhanced performance of TBPh-based COFs over TPh-based COFs is attributed to the additional phenyl units in TBPh, which enable stronger π interactions with cationic RhB dye molecules, as depicted in Fig. 9**(a)**. Furthermore, the positively charged RhB is electrostatically attracted to the negatively polarized sites on the TFP COF surface [89]. FTIR spectra recorded after RhB binding to TFP–TBPh (I) reveal shifts in characteristic vibrational bands, providing direct evidence of these specific adsorbent-dye interactions [**Fig. S18**]. As shown in **Fig. S19**, isotherm experiments of RhB adsorption were conducted at varying concentrations, and a saturation curve was plotted to determine the maximum adsorption capacity ($q_{\max}$), as summarized in **Table S9**. The adsorption capacity values of RhB onto TFP-TPh (I), TFP-TPh (II), TFP-TBPh (I), and TFP-TBPh (II) COFs were 127, 238, 155, and 243 mg/g, respectively. Temperature-dependent studies of TFP–TBPh (II) reveal that its adsorption capacity increases with rising temperature, indicating an endothermic adsorption process [**Fig. S20**]. The fitting degrees (R^2) of TFP-TBPh (I) and (II) COFs to the Langmuir and Freundlich isotherm models [90] were 0.9813 and 0.9152, respectively [Fig. 9**(d) and (e)**]. Similarly, TFP-TPh (I) and (II) COFs exhibited a higher fitting degree to the Langmuir model compared to the Freundlich model. This suggests that when the Langmuir model provides a better fit, the adsorption process is predominantly monolayer, typically observed in adsorbents with well-structured surfaces that facilitate chemisorption through functionalized units. Importantly, the TFP–TBPh (II) COF also demonstrates good recyclability: after five

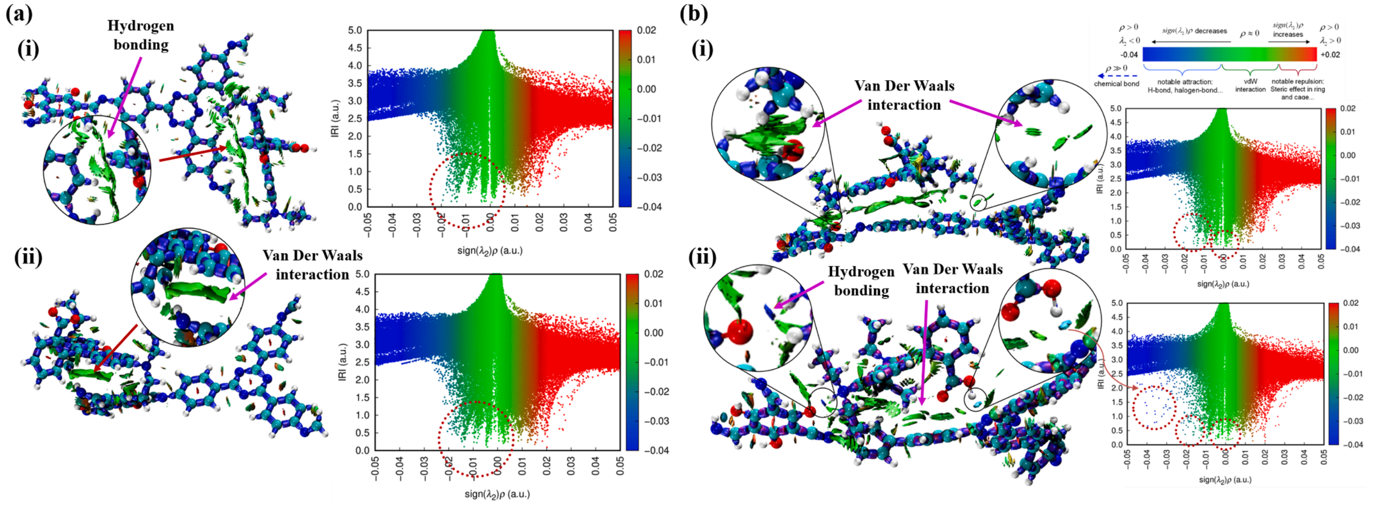

Fig. 10. The 3D isosurfaces and 2D scatter graphs of (a) TFP-TPh@RhB and (b) TFP-TBPh@ RhB complexes.

adsorption–desorption cycles, its RhB uptake capacity decreased by only 19 %, maintaining approximately 78 % removal efficiency [Fig. S21]. Interestingly, the FTIR and XRD analyses demonstrated that both TFP-TPh (I) and TFP-TBPh (I) maintained their characteristic absorption bands and crystalline structures even after the adsorption of RhB, as shown in Figs. S22 and S23. This indicates that the framework structures of the COFs remained stable and intact during the adsorption process. Moreover, for practical real application, the adsorption performance of TFP TBPh (II), which demonstrated the highest capacity under standard conditions, was evaluated under simulated industrial wastewater environments. A noticeable decline in adsorption efficiency was observed, likely due to the presence of various substances in the wastewater that interacted with TFP TBPh (II) through multiple forces, consequently weakening its affinity for RhB, as shown in Fig. S24 and Table S10.

The QTAIM topological analysis further supports the nature of interactions between RhB and the units of TFP COFs. As summarized in Table S11, two orientations of RhB were examined for TFP-TPh and TFP-TBPh COFs, denoted as (i) and (ii), and their interaction geometries are illustrated in Fig. S25 [91,92]. From the data in Table S11 and Fig. S25, it is evident that in the TFP-TPh@RhB complexes, multiple noncovalent interactions form between the dye molecules and the TPh-based framework. These are characterized by topological indicators such as $\nabla^2\rho > 0$ and $H_r > 0$, with $-G_r/V_r > 1$, signifying predominantly electrostatic, open-shell interactions typical of van der Waals forces. A similar interaction profile is observed in the TFP-TBPh@RhB systems, reinforcing the conclusion that electrostatic attractions play a central role in dye binding. Interestingly, for the TFP-TBPh@RhB (i) configuration, a distinctive N-H···O hydrogen bond is identified, with topological parameters showing $H_r < 0$ and $-G_r/V_r < 1$. These values are consistent with covalent-like, closed-shell hydrogen bonding. This observation underscores the enhanced binding affinity of the TBPh-based framework, where π-rich biphenyl units and accessible hydrogen-bond donors contribute to dual-mode interaction mechanisms, both Van Der Waals and hydrogen bonding. Overall, these results reveal that TFP-TBPh COFs exhibit a stronger and more diverse set of noncovalent interactions with RhB than their TPh counterparts, positioning them as more effective materials for dye adsorption applications. For RhB adsorption, IRI analysis was conducted on two distinct dye orientations [(i) and (ii)] for each COF framework [Fig. 10]. In the TFP–TPh@RhB systems, both configurations display green IRI isosurfaces at the dye-framework interface, signifying predominant Van Der Waals stabilization. The (ii) orientation, however, presents a thicker and smoother green region, reflecting a larger contact area and more favorable dye alignment. In contrast, the TFP–TBPh@RhB complexes exhibit a mixture of interaction types. In the (i) orientation, only green dispersion regions are observed, indicating that the heteroatoms of the dye remain too distant for hydrogen bonding. In the (ii) orientation, distinct blue isosurfaces appear between the oxygen of the dye and nitrogen atoms and the hydrogen atoms of the framework, signifying the formation of N-H···O hydrogen bonds, alongside green dispersion regions. The associated scatter plots show spikes at −0.04 and −0.02 a.u., typical of hydrogen bonding, together with the zero-centered dispersion peak. Overall, IRI mapping demonstrates that Van Der Waals forces govern guest binding in all TFP COF@CO_2 and TFP COF@RhB assemblies, while TBPh-based COFs in the (ii) orientation uniquely facilitate dual-mode interactions incorporating both hydrogen bonds and dispersion contacts. This dual interaction mechanism underpins the superior adsorption performance of TBPh-based frameworks.

4. Conclusions

This study successfully developed triazine-based porous materials, TFP-TPh (I) and TFP-TBPh (I), COFs using Schiff-base reactions, along with mesoporous silica-template-derived TFP-TPh (II) and TFP-TBPh (II) COFs. TFP-TBPh (I) COF demonstrated remarkable properties, including a high specific surface area of 904 m^2 g^{-1} and thermal stability (T_{d10}: 569 °C, char yield: 64.6 wt%), while TFP-TPh (I) COF achieved a CO_2 capture capacity of 4.09 mmol g^{-1} at 273 K. Furthermore, TFP-TBPh (II) COF showed exceptional dye adsorption performance, removing 86.04 % of RhB within 10 s. The pseudo-second-order model provided the best fit, highlighting that the adsorption process is primarily governed by chemisorption, which is predominantly attributed to the presence of triazine units in these materials.

CRediT authorship contribution statement

Yang-Chin Kao: Writing – original draft, Formal analysis, Data curation, Conceptualization. **Kuan-Ting Yeh:** Formal analysis, Data curation, Conceptualization. **Mohamed Gamal Mohamed:** Writing – review & editing, Writing – original draft, Supervision, Methodology, Data curation, Conceptualization. **Hira Karim:** Software. **Wei-Hung Su:** Supervision. **Shiao-Wei Kuo:** Supervision, Resources, Project administration.

Declaration of competing interest

Acknowledgments

This study was supported financially by the National Science and Technology Council, Taiwan, under contracts NSTC 113-2223-E-110-001- and 113-2221-E-110-012-MY3. The authors thank the staff at National Sun Yat-sen University for their assistance with the TEM (ID: EM022600) experiments.

Appendix A. Supplementary data

Supplementary data to this article can be found online at https://doi.org/10.1016/j.seppur.2025.133827.

Data availability

The data that has been used is confidential.

References

[1] M. Shabir, M. Yasin, M. Hussain, I. Shafiq, P. Akhter, A.S. Nizami, B.H. Jeon, Y. K. Park, A review on recent advances in the treatment of dye-polluted wastewater, J. Ind. Eng. Chem. 112 (2022) 1–19, https://doi.org/10.1016/j.jiec.2022.05.013.

[2] A. Tkaczyk, K. Mitrowska, A. Posyniak, Synthetic organic dyes as contaminants of the aquatic environment and their implications for ecosystems: a review, Sci. Total Environ. 717 (2020) 137222, https://doi.org/10.1016/j.scitotenv.2020.137222.

[3] R. Al-Tohamy, S.S. Ali, F. Li, K.M. Okasha, Y.A.G. Mahmoud, T. Elsamahy, H. Jiao, Y. Fu, J. Sun, A critical review on the treatment of dye-containing wastewater: ecotoxicological and health concerns of textile dyes and possible remediation approaches for environmental safety, Ecotoxicol. Environ. Saf. 231 (2022) 113160, https://doi.org/10.1016/j.ecoenv.2021.113160.

[4] H. Kolya, C.W. Kang, Toxicity of metal oxides, dyes, and dissolved organic matter in water: implications for the environment and human health, Toxics 12 (2024) 111, https://doi.org/10.3390/toxics12020111.

[5] L.J. Nunes, The rising threat of atmospheric CO_2: a review on the causes, impacts, and mitigation strategies, Environments 10 (2023) 66, https://doi.org/10.3390/environments10040066.

[6] M. Kabir, U.E. Habiba, W. Khan, A. Shah, S. Rahim, R. Patricio, L. Ali, M. Shafiq, Climate change due to increasing concentration of carbon dioxide and its impacts on environment in 21st century; a mini review, J. King Saud Univ. Sci. 35 (2023) 102693, https://doi.org/10.1016/j.jksus.2023.102693.

[7] N. Bahman, D. Alalaiwat, Z. Abdulmohsen, M. Al Khalifa, S. Al Baharna, M.A. Al-Mannai, A. Younis, A critical review on global CO_2 emission: where do industries stand? REVEH 38 (2023) 681–696, https://doi.org/10.1515/reveh-2022-0105.

[8] M.G. Kotp, S.W. Kuo, Selective capturing of the CO_2 emissions utilizing ecological (3-mercaptopropyl) trimethoxysilane-coated porous organic Polymers in composite materials, Polymers 16 (2024) 1759, https://doi.org/10.3390/polym16131759.

[9] M.G. Mohamed, C.C. Chen, M. Ibrahim, A.O. Mousa, M.H. Elsayed, Y. Ye, S.W. Kuo, Tetraphenylanthraquinone and dihydroxybenzene-tethered conjugated microporous polymer for enhanced CO_2 uptake and supercapacitive energy storage, JACS Au 4 (2024) 3593–3605, https://doi.org/10.1021/jacsau.4c00537.

[10] M. Ejaz, M.G. Mohamed, S.W. Kuo, Solid state chemical transformation provides a fully benzoxazine-linked porous organic polymer displaying enhanced CO_2 capture and supercapacitor performance, Polym. Chem. 14 (2023) 2494–2509, https://doi.org/10.1039/D3PY00158J.

[11] L. Yang, Y. Sun, R. Yu, P. Huang, Q. Zhou, H. Yang, S. Lin, H. Zeng, Urchin-like CO_2-responsive magnetic microspheres for highly efficient organic dye removal, J. Hazard. Mater. 469 (2024) 134101, https://doi.org/10.1016/j.jhazmat.2024.134101.

[12] H. Liu, B. Wang, H. Liu, Y. Zheng, M. Li, K. Tang, B. Pan, C. Liu, J. Luo, X. Pang, Multi-crosslinked robust alginate/polyethyleneimine modified graphene aerogel for efficient organic dye removal, Colloids Surf. A: Physicochem. Eng. Asp. 683 (2024) 133034, https://doi.org/10.1016/j.colsurfa.2023.133034.

[13] C. Cui, D. Li, L. Wang, Y. Wang, Curdlan/sodium carboxymethylcellulose composite adsorbents: a biodegradable solution for organic dye removal from water, Carbohydr. Polym. 328 (2024) 121737, https://doi.org/10.1016/j.carbpol.2023.121737.

[14] L. Khezami, M.A.B. Aissa, A. Modwi, A. Guesmi, F.K. Algethami, M. Bououdina, Efficient removal of organic dyes by Cr-doped ZnO nanoparticles, Biomass. Convers. Biorefin. 14 (2024) 4177–4190, https://doi.org/10.1007/s13399-022-02952-w.

[15] Z. Zhang, M. Zhang, X. Zhao, J. Cao, High-efficient removal and adsorption mechanism of organic dyes in wastewater by KOH-activated biochar from phenol-formaldehyde resin modified wood, Sep. Purif. Technol. 330 (2024) 125542, https://doi.org/10.1016/j.seppur.2023.125542.

[16] M.F. Lanjwani, M. Tuzen, M.Y. Khuhawar, T.A. Saleh, Trends in photocatalytic degradation of organic dye pollutants using nanoparticles: a review, Inorg. Chem. Commun. 159 (2024) 111613, https://doi.org/10.1016/j.inoche.2023.111613.

[17] C.W. Huang, S.R. Zhou, W.C. Hsiao, Multifunctional TiO_2/MIL-100 (Fe) to conduct adsorption, photocatalytic, and heterogeneous photo-Fenton reactions for removing organic dyes, J. Taiwan Inst. Chem. Eng. 158 (2024) 104850, https://doi.org/10.1016/j.jtice.2023.104850.

[18] S.Y. Chen, Y.F. Deng, T. Huang, N. Zhang, Y. Wang, Polydopamine-assisted MXene decoration on electrospun polylactide fibers toward oil/water separation and organic dye adsorption, Sep. Purif. Technol. 328 (2024) 125040, https://doi.org/10.1016/j.seppur.2023.125040.

[19] H. Su, W. Qiu, T. Deng, X. Zheng, H. Wang, P. Wen, Fabrication of physically multi-crosslinked sodium alginate/carboxylated-chitosan/montmorillonite-base aerogel modified by polyethyleneimine for the efficient adsorption of organic dye and Cu (II) contaminants, Sep. Purif. Technol. 330 (2024) 125321, https://doi.org/10.1016/j.seppur.2023.125321.

[20] J.M. Dias, M.C. Alvim-Ferraz, M.F. Almeida, J. Rivera-Utrilla, M. Sánchez-Polo, Waste materials for activated carbon preparation and its use in aqueous-phase treatment: a review, J. Environ. Manag. 85 (2007) 833–846, https://doi.org/10.1016/j.jenvman.2007.07.031.

[21] A. Alabadi, S. Razzaque, Y. Yang, S. Chen, B. Tan, Highly porous activated carbon materials from carbonized biomass with high CO_2 capturing capacity, Chem. Eng. J. 281 (2015) 606–612, https://doi.org/10.1016/j.cej.2015.06.032.

[22] L.R. Rad, M. Anbia, Zeolite-based composites for the adsorption of toxic matters from water: a review, J. Environ. Chem. Eng. 9 (2021) 106088, https://doi.org/10.1016/j.jece.2021.106088.

[23] E. Pérez-Botella, S. Valencia, F. Rey, Zeolites in adsorption processes: state of the art and future prospects, Chem. Rev. 122 (2022) 17647–17695, https://doi.org/10.1021/acs.chemrev.2c00140.

[24] L. Shi, K.O. Kirlikovali, Z. Chen, O.K. Farha, Metal-organic frameworks for water vapor adsorption, Chem 10 (2024) 484–503, https://doi.org/10.1016/j.chempr.2023.09.005.

[25] N.A.H. Alshammari, J.S. Alnawmasi, A.M. Alotaibi, O.A. Alshammari, M. A. Abomuti, N.H. Elsayed, A.A. El-Bindary, Efficient adsorption of fluorescein dye from aqueous solutions by Al/Th-MOF bimetal-organic frameworks: adsorption isotherm, kinetics, DFT computation, and optimization via box-behnken design, Process Saf. Environ. Prot. 190 (2024) 353–371, https://doi.org/10.1016/j.psep.2024.08.037.

[26] M.G. El-Desouky, A.A. Alayyafi, G.A. Al-Hazmi, A.A. El-Bindary, Effect of metal organic framework alginate aerogel composite sponge on adsorption of tartrazine from aqueous solutions: adsorption models, thermodynamics and optimization via box-behnken design, J. Mol. Liq. 399 (2024) 124392, https://doi.org/10.1016/j.molliq.2024.124392.

[27] M.M. Samy, M.G. Mohamed, S.U. Sharma, S.V. Chaganti, J.T. Lee, S.W. Kuo, An ultrastable tetrabenzonaphthalene-linked conjugated microporous polymer functioning as a high-performance electrode for supercapacitors, J. Taiwan Inst. Chem. Eng. 158 (2024) 104750, https://doi.org/10.1016/j.jtice.2023.104750.

[28] S.Y. Chang, A.M. Elewa, M.G. Mohamed, I.M.A. Mekhemer, M.M. Samy, K. Zhang, H.H. Chou, S.W. Kuo, Rational design and synthesis of bifunctional dibenzo [g, p] chrysene-based conjugated microporous polymers for energy storage and visible light-driven photocatalytic hydrogen evolution, Mater. Today Chem. 33 (2023) 101680, https://doi.org/10.1016/j.mtchem.2023.101680.

[29] M.G. Mohamed, S.U. Sharma, P.T. Wang, M. Ibrahim, M.H. Lin, C.L. Liu, M. Ejaz, H.J. Yen, S.W. Kuo, Construction of fully π-conjugated, diyne-linked conjugated microporous polymers based on tetraphenylethene and dibenzo [g, p] chrysene units for energy storage, Polym. Chem. 15 (2024) 2827–2839, https://doi.org/10.1039/D4PY00421C.

[30] A.O. Mousa, Z.I. Lin, S.V. Chaganti, C.H. Chuang, C.K. Chen, S.W. Kuo, M. G. Mohamed, Bifunctional imidazolium linked tetraphenylethene based conjugated microporous polymers for dynamic antibacterial properties and supercapacitor electrodes, Polym. Chem. 15 (2024) 397–411, https://doi.org/10.1039/D3PY01303K.

[31] M.G. Mohamed, W.C. Chang, S.W. Kuo, Crown ether-and benzoxazine-linked porous organic polymers displaying enhanced metal ion and CO_2 capture through solid-state chemical transformation, Macromolecules 55 (2022) 7879–7892, https://doi.org/10.1021/acs.macromol.2c01216.

[32] M.G. Mohamed, A.F.M. EL-Mahdy, M.G. Kotp, S.W. Kuo, Advances in porous organic polymers: syntheses, structures, and diverse applications, Mater. Adv. 3 (2022) 707–733, https://doi.org/10.1039/D1MA00771H.

[33] M.M. Samy, I.M.A. Mekhemer, M.G. Mohamed, M.H. Elsayed, K.H. Lin, Y.K. Chen, T.L. Wu, H.H. Chou, S.W. Kuo, Conjugated microporous polymers incorporating thiazolo [5, 4-d] thiazole moieties for sunlight-driven hydrogen production from water, Chem. Eng. J. 446 (2022) 137158, https://doi.org/10.1016/j.cej.2022.137158.

[34] A.M. Elewa, A.F.M. EL-Mahdy, M.H. Elsayed, M.G. Mohamed, S.W. Kuo, H. H. Chou, Sulfur-doped triazine-conjugated microporous polymers for achieving the robust visible-light-driven hydrogen evolution, Chem. Eng. J. 421 (2021) 129825, https://doi.org/10.1016/j.cej.2021.129825.

[35] W.T. Chung, I.M.A. Mekhemer, M.G. Mohamed, A.M. Elewa, A.F.M. EL-Mahdy, H. H. Chou, S.W. Kuo, K.C.W. Wu, Recent advances in metal/covalent organic frameworks based materials: their synthesis, structure design and potential applications for hydrogen production, Coord. Chem. Rev. 483 (2023) 215066, https://doi.org/10.1016/j.ccr.2023.215066.

[36] I.M.A. Mekhemer, M.M. Elsenety, A.M. Elewa, K.D.G. Huynh, M.M. Samy, M. G. Mohamed, D.M. Dorrah, D.C.K. Hoang, A.F. Musa, S.W. Kuo, H.H. Chou, Push–pull–pull interactions of 2D imide–imine-based covalent organic framework to promote charge separation in photocatalytic hydrogen production, J. Mater. Chem. A 12 (2024) 10790–10798, https://doi.org/10.1039/D4TA01108B.

[37] A. Knebel, J. Caro, Metal–organic frameworks and covalent organic frameworks as disruptive membrane materials for energy-efficient gas separation, Nat. Nanotechnol. 17 (2022) 911–923, https://doi.org/10.1038/s41565-022-01168-3.

[38] R. Shah, S. Ali, F. Raziq, S. Ali, P.M. Ismail, S. Shah, R. Iqbal, X. Wu, W. He, X. Zu, Exploration of metal organic frameworks and covalent organic frameworks for energy-related applications, Coord. Chem. Rev. 477 (2023) 214968, https://doi.org/10.1016/j.ccr.2022.214968.

[39] W. Zhang, L. Chen, S. Dai, C. Zhao, C. Ma, L. Wei, M. Zhu, S.Y. Chong, H. Yang, L. Liu, Reconstructed covalent organic frameworks, Nature 604 (2022) 72–79, https://doi.org/10.1038/s41586-022-04443-4.

[40] M. Ma, X. Lu, Y. Guo, L. Wang, X. Liang, Combination of metal-organic frameworks (MOFs) and covalent organic frameworks (COFs): recent advances in synthesis and analytical applications of MOF/COF composites, TrAC, Trends Anal. Chem. 157 (2022) 116741, https://doi.org/10.1016/j.trac.2022.116741.

[41] W. Lee, H. Li, Z. Du, D. Feng, Ion transport mechanisms in covalent organic frameworks: implications for technology, Chem. Soc. Rev., 53 (2024) 8182–8201, https://doi.org/10.1039/D4CS00409D.

[42] L. Xiao, L. Qi, J. Sun, A. Husile, S. Zhang, Z. Wang, J. Guan, Structural regulation of covalent organic frameworks for advanced electrocatalysis, Nano Energy 120 (2024) 109155, https://doi.org/10.1016/j.nanoen.2023.109155.

[43] M. Lu, S.B. Zhang, R.H. Li, L.Z. Dong, M.Y. Yang, P. Huang, Y.F. Liu, Z.H. Li, H. Zhang, M. Zhang, S.L. Li, Y.Q. Lan, 3D covalent organic frameworks with 16-connectivity for photocatalytic C (sp^3)–C (sp^2) cross-coupling, J. Am. Chem. Soc. 146 (2024) 25832–25840, https://doi.org/10.1021/jacs.4c08951.

[44] A. Basit, Y.C. Kao, Y.A. El-Ossaily, S.W. Kuo, M.G. Mohamed, Rational engineering and synthesis of pyrene and thiazolo [5,4-d] thiazole-functionalized conjugated microporous polymers for efficient supercapacitor energy storage, J. Mater. Chem. A 12 (2024) 30508–30521, https://doi.org/10.1039/D4TA05908E.

[45] M. Ejaz, M.G. Mohamed, W.C. Huang, S.W. Kuo, Pyrene-based covalent organic polymers with nano carbonaceous composites for efficient supercapacitive energy storage, J. Mater. Chem. A 11 (2023) 22868–22883, https://doi.org/10.1039/D3TA02741D.

[46] M.G. Mohamed, C.C. Lee, A.F.M. EL-Mahdy, J. Lüder, M.H. Yu, Z. Li, Z. Zhu, C. C. Chueh, S.W. Kuo, Exploitation of two-dimensional conjugated covalent organic frameworks based on tetraphenylethylene with bicarbazole and pyrene units and applications in perovskite solar cells, J. Mater. Chem. A 8 (2020) 11448–11459, https://doi.org/10.1039/D0TA02956D.

[47] S.W. Kuo, Hydrogen bonding mediated self-assembled structures from block copolymer mixtures to mesoporous materials, Polym. Int. 71 (2022) 393–410, https://doi.org/10.1002/pi.6264.

[48] M.G. Mohamed, E.C. Atayde Jr, B.M. Matsagar, J. Na, Y. Yamauchi, K.C.W. Wu, S. W. Kuo, Construction hierarchically mesoporous/microporous materials based on block copolymer and covalent organic framework, J. Taiwan Inst. Chem. Eng. 112 (2020) 180–192, https://doi.org/10.1016/j.jtice.2020.06.013.

[49] T.C. Chou, W.C. Chen, M.G. Mohamed, Y.C. Huang, S.W. Kuo, Organic-Inorganic Phenolic/POSS hybrids provide highly ordered mesoporous structures templated by high thermal stability of PS-*b*-P4VP diblock copolymer, Chem. Eur. J. 29 (2023) e202300538, https://doi.org/10.1002/chem.202300538.

[50] M.G. Mohamed, S.W. Kuo, Progress in the self-assembly of organic/inorganic polyhedral oligomeric silsesquioxane (POSS) hybrids, Soft Matter 18 (2022) 5535–5561, https://doi.org/10.1039/D2SM00635A.

[51] W.C. Chu, S.F. Chiang, J.G. Li, S.W. Kuo, Mesoporous silicas templated by symmetrical multiblock copolymers through evaporation-induced self-assembly, RSC Adv. 4 (2014) 784–793, https://doi.org/10.1039/C3RA45348K.

[52] J. Zhao, J. Chen, M. Zhou, Q. Zhang, X. Li, J. Pan, Ultra-firm phthalocyanine-based tetragonal covalent organic framework layer@ nano silicon anode for high durability Li-ion battery, Chem. Eng. J. 488 (2024) 151110, https://doi.org/10.1016/j.cej.2024.151110.

[53] L. Xu, L. Zheng, Y. Jing, X. Guo, X. Hu, B. Xu, S. Zhang, Hexagonal 2D covalent organic frameworks from nonpolar and symmetric electron-accepting substituents for electron transport layers in near-infrared PeLEDs, J. Mater. Chem. A 12 (2024) 286–292, https://doi.org/10.1039/D3TA05200A.

[54] R. Li, X. Tang, J. Wu, K. Zhang, Q. Zhang, J. Wang, J. Zheng, S. Zheng, J. Fan, W. Zhang, X. Li, S. Cai, A sulfonate-functionalized covalent organic framework for record-high adsorption and effective separation of organic dyes, Chem. Eng. J. 464 (2023) 142706, https://doi.org/10.1016/j.cej.2023.142706.

[55] X. Wu, X. Tang, K. Zhang, C. Harrod, R. Li, J. Wu, X. Yang, S. Zheng, J. Fan, W. Zhang, X. Li, S. Cai, Tuning the topology of two-dimensional covalent organic frameworks through site-selective synthetic strategy, Chem. Eur. J. 30 (2024) e202303781, https://doi.org/10.1002/chem.202303781.

[56] R.E. Mow, G.A. Russell-Parks, G.E. Redwine, B.E. Petel, T. Gennett, W. A. Braunecker, Polymer-coated covalent organic frameworks as porous liquids for gas storage, Chem. Mat. 36 (2024) 1579–1590, https://doi.org/10.1021/acs.chemmater.3c02828.

[57] Y. Qian, H.L. Jiang, Structural regulation of covalent organic frameworks for catalysis, Acc. Chem. Res. 57 (2024) 1214–1226, https://doi.org/10.1021/acs.accounts.4c00061.

[58] E.A. Ardakani, M. Rahmani, A. Hosseinian, S.B. Ghaffari, M.H. Sarrafzadeh, Improvement strategies on application of covalent organic frameworks in adsorption, photocatalytic, and membrane processes for organic pollution removal from water, Coord. Chem. Rev. 518 (2024) 216087, https://doi.org/10.1016/j.ccr.2024.216087.

[59] R. Li, F. Sun, Z. Liu, Y. Shi, S. He, J. Chen, Research progress and prospect of Covalent Organic Frameworks (COFs) and composites: from synthesis to application in water contaminants, J. Environ. Chem. Eng. (2024) 113944, https://doi.org/10.1016/j.jece.2024.113944.

[60] I. Ahmed, G. Lee, H.J. Lee, S.H. Jhung, Adsorption of pharmaceuticals from water using metal-organic frameworks (MOFs), MOF-derived carbons, covalent-organic frameworks (COFs), COF-derived carbons: comparison of the four adsorbents, Chem. Eng. J. 448 (2024) 151022, https://doi.org/10.1016/j.cej.2024.151022.

[61] J.H. Wang, T.A. Gaber, S.W. Kuo, A.F.M. EL-Mahdy, π-electron-extended triazine-based covalent organic framework as photocatalyst for organic pollution degradation and H_2 production from water, Polymers 15 (2023) 1685, https://doi.org/10.3390/polym15071685.

[62] J. Wu, J. Liu, B. Wen, Y. Li, B. Zhou, Z. Wang, S. Yang, R. Zhao, Nitrogen-rich covalent triazine frameworks for high-efficient removal of anion dyes and the synergistic adsorption of cationic dyes, Chemosphere 272 (2021) 129622, https://doi.org/10.1016/j.chemosphere.2021.129622.

[63] C. Xu, J. Wang, B. Gao, M. Dou, R. Chen, Synergistic adsorption and visible-light catalytic degradation of RhB from recyclable 3D mesoporous graphitic carbon nitride/reduced graphene oxide aerogels, J. Mater. Sci. 54 (2019) 8892–8906, https://doi.org/10.1007/s10853-019-03531-7.

[64] Y. Zhuang, Q. Zhu, G. Li, Z. Wang, P. Zhan, C. Ren, Z. Si, S. Li, D. Cai, P. Qin, Photocatalytic degradation of organic dyes using covalent triazine-based framework, Mater. Res. Bull. 146 (2022) 111619, https://doi.org/10.1016/j.materresbull.2021.111619.

[65] G. Lee, I. Ahmed, S.H. Jhung, CO_2 adsorption using functionalized metal–organic frameworks under low pressure: contribution of functional groups, excluding amines, to adsorption, Chem. Eng. J. 481 (2024) 148440, https://doi.org/10.1016/j.cej.2023.148440.

[66] S. Guo, Z. Zou, Y. Chen, X. Long, M. Liu, X. Li, J. Tan, R. Chen, Synergistic effect of hydrogen bonding and π-π interaction for enhanced adsorption of rhodamine B from water using corn straw biochar, Environ. Pollut. 320 (2023) 121060, https://doi.org/10.1016/j.envpol.2023.121060.

[67] E. Kashi, S. Surip, T. Khadiran, W.I. Nawawi, Y. De Luna, Z.M. Yaseen, A.H. Jawad, High adsorptive performance of chitosan-microalgae-carbon-doped TiO_2 (kronos)/salicylaldehyde for brilliant green dye adsorption: optimization and mechanistic approach, Int. J. Biol. Macromol. 259 (2024) 129147, https://doi.org/10.1016/j.ijbiomac.2023.129147.

[68] N.I. Normi, A.S. Abdulhameed, A.H. Jawad, S.N. Surip, R. Razuan, M.L. Ibrahim, Hydrothermal-assisted grafting of schiff base chitosan by salicylaldehyde for adsorptive removal of acidic dye: statistical modeling and adsorption mechanism, J. Environ. Polym. Degrad. 31 (2023) 1925–1937, https://doi.org/10.1007/s10924-022-02730-9.

[69] D. Wei, J. Li, M. Guo, J. Xu, Q. Deng, X. Wang, Rational selection of 4, 4′, 4″-(1, 3, 5-triazine-2, 4, 6-triyl) trianiline-based covalent organic framework as adsorbent for effective co-extraction of aflatoxins, zearalenone and its metabolites from food and biological samples, Food Chem. 463 (2025) 141013, https://doi.org/10.1016/j.foodchem.2024.141013.

[70] Y. Kumar, I. Ahmad, A. Rawat, R.K. Pandey, P. Mohanty, R. Pandey, Flexible linker-based triazine-functionalized 2D covalent organic frameworks for supercapacitor and gas sorption applications, ACS Appl. Mater. Interfaces 16 (2024) 11605–11616, https://doi.org/10.1021/acsami.4c00126.

[71] Q. Yang, Y. Liu, L. Xiang, J. Zhang, Y. Yin, F. Xu, Y. Mai, A general synthetic method towards conjugated microporous polymers with ordered bicontinuous mesostructures, Chem. Commun. 59 (2023) 4742–4745, https://doi.org/10.1039/D3CC00481C.

[72] W. Li, H.X. Jiang, M.F. Cui, R. Wang, A.N. Tang, D.M. Kong, SiO_2 templates-derived hierarchical porous COFs sample pretreatment tool for non-targeted analysis of chemicals in foods, J. Hazard. Mater. 432 (2022) 128705, https://doi.org/10.1016/j.jhazmat.2022.128705.

[73] U. Koch, P.L.A. Popelier, Characterization of CHO hydrogen bonds on the basis of the charge density, J. Phys. Chem. 99 (1995) 9747–9754, https://doi.org/10.1021/j100024a016.

[74] P.L.A. Popelier, Characterization of a dihydrogen bond on the basis of the electron density, J. Phys. Chem. A 102 (1998) 1873–1878, https://doi.org/10.1021/jp9805048.

[75] H. Hashemzadeh, H. Raissi, Loading and release of anticancer drug from phosphorene as a template material with high efficient carrier: from vacuum to cell membrane, J. Mol. Liq. 291 (2019) 111346, https://doi.org/10.1016/j.molliq.2019.111346.

[76] Z. Hasanzade, H. Raissi, Investigation of graphene-based nanomaterial as nanocarrier for adsorption of paclitaxel anticancer drug: a molecular dynamics simulation study, J. Mol. Model. 23 (2017) 1–8, https://doi.org/10.1007/s00894-017-3207-1.

[77] M. Shahabi, H. Raissi, Assessment of solvent effects on the inclusion behavior of pyrazinamide drug into cyclic peptide based nanotubes as novel drug delivery vehicles, J. Mol. Liq. 268 (2018) 326–334, https://doi.org/10.1016/j.molliq.2018.07.064.

[78] H. Karim, S. Sardar, A. Mumtaz, A. Tabassum, M. Arfan, A. Mahmood, J. M. Leveque, C.D. Wilfred, S.F. Adil, M.R. Hatshan, M. Khan, Unravelling the role of non-covalent interactions using imidazolium and amino acid based organic salts for efficient CO_2 capture: experimental, DFT and COSMO-RS explorations, J. Environ. Chem. Eng. 13 (2025) 116237, https://doi.org/10.1016/j.jece.2025.116237.

[79] H. Wang, H. Wang, G. Liu, Q. Yan, In-situ pyrolysis of taihu blue algae biomass as appealing porous carbon adsorbent for CO_2 capture: role of the intrinsic N, Sci. Total Environ. 771 (2021) 145424, https://doi.org/10.1016/j.scitotenv.2021.145424.

[80] K. Zhu, Q. Wei, H. Li, X. Ren, Recovery of titanium from ilmenite HCl leachate using a hydrophobic deep eutectic solvent, ACS Sustain. Chem. Eng. 10 (2022) 2125–2135, https://doi.org/10.1021/acssuschemeng.1c07204.

[81] A. Sagaama, N. Issaoui, O. Al-Dossary, A.S. Kazachenko, M.J. Wojcik, Non covalent interactions and molecular docking studies on morphine compound, J. King Saud Univ. Sci. 33 (2021) 101606, https://doi.org/10.1016/j.jksus.2021.101606.

[82] J. Liu, W.L. Zhai, Y. Wang, Y.T. Ye, Z.C. Qin, J. Duan, Q. Li, W. Zhu, RhB intercalated Zr (VI)-bipyridine architecture for efficient ratiometric fluorescent response toward Cr (VI) analyte and decontamination of Cr (VI) and reactive dye via photochemical REDOX, J. Mol. Struct. 1325 (2025) 141008, https://doi.org/10.1016/j.molstruc.2024.141008.

[83] X. Zhang, W. Liu, F. Han, L. Jiang, Z. Li, Composite of titanium dioxide and hydrogen-bonded organic framework− a dye-sensitized photocatalyst, Appl. Surf. Sci. 644 (2024) 158770, https://doi.org/10.1016/j.apsusc.2023.158770.

[84] Y.S. Wang, T.R. Huo, Y. Wang, J.W. Bai, P.P. Huang, C. Li, S.Y. Deng, H. Mei, J. Qian, X.C. Zhang, C. Ding, Q.Y. Zhang, Constructing mesoporous biochar derived from waste carton: improving multi-site adsorption of dye wastewater and investigating mechanism, Environ. Res. 242 (2024) 117775, https://doi.org/10.1016/j.envres.2023.117775.

[85] M. Wang, R. Yan, M. Shan, S. Liu, H. Tang, Fabrication of crown ether-containing copolymer porous membrane and their enhanced adsorption performance for cationic dyes: experimental and DFT investigations, Chemosphere 352 (2024) 141363, https://doi.org/10.1016/j.chemosphere.2024.141363.

[86] A. Lv, X. Lv, X. Xu, Z.B. Shao, Tailored ultra-tough, antimicrobial and recyclable hydrogels based on chitosan and ionic liquid modified montmorillonite with different chain lengths for efficient adsorption of organic dyes in wastewater, Int. J. Biol. Macromol. 257 (2024) 128752, https://doi.org/10.1016/j.ijbiomac.2023.128752.

[87] Y.S. Ho, G. McKay, Pseudo-second order model for sorption processes, Process Biochem. 34 (1999) 451–465, https://doi.org/10.1016/S0032-9592(98)00112-5.

[88] R. Ezzati, M. Azizi, S. Ezzati, A theoretical approach for evaluating the contributions of pseudo-first-order and pseudo-second-order kinetics models in the langmuir rate equation, Vacuum 222 (2024) 113018, https://doi.org/10.1016/j.vacuum.2024.113018.

[89] R. Ezzati, S. Ezzati, M. Azizi, Exact solution of the langmuir rate equation: new insights into pseudo-first-order and pseudo-second-order kinetics models for adsorption, Vacuum 220 (2024) 112790, https://doi.org/10.1016/j.vacuum.2023.112790.

[90] R. Li, K. Zhang, X. Yang, R. Xiao, Y. Xie, X. Tang, G. Miao, J. Fan, W. Zhang, S. Zheng, S. Cai, Construction of a carboxyl-functionalized clover-like covalent organic framework for selective adsorption of organic dyes, Sep. Purif. Technol. 340 (2024) 126765, https://doi.org/10.1016/j.seppur.2024.126765.

[91] I.X. García-Zubiri, G. González-Gaitano, Sorption models in cyclodextrin polymers: langmuir, freundlich, and a dual-mode approach, J. R. Isasi, J. Colloid Interface Sci. 337 (2009) 11–18, https://doi.org/10.1016/j.jcis.2009.04.07.

[92] M. Zeeshan, T. Javed, C. Kumari, A. Thumma, M. Wasim, M.B. Taj, I. Sharma, M. N. Haider, M. Batool, Investigating the Interactions between dyes and porous/composite materials: a comprehensive study, Sustain. Chem. Environ. 9 (2025) 100217, https://doi.org/10.1016/j.scenv.2025.100217.